Optimization of Optical Nonlinearities in Quantum Cascade Lasers

A Dissertation
Presented to
The Academic Faculty

By

Jing Bai

In Partial Fulfillment
Of the Requirements for the Degree
Doctor of Philosophy in Electrical and Computer Engineering

Georgia Institute of Technology

December 2007

Optimization of Optical Nonlinearities in Quantum Cascade Lasers

Apporved by:

Professor David S. Citrin, Advisor
School of Electrical and Computer Engineering
Georgia Institute of Technology

Professor Russell D. Dupuis
School of Electrical and Computer Engineering
Georgia Institute of Technology

Professor Gee-Kung Chang
School of Electrical and Computer Engineering
Georgia Institute of Technology

Professor Phillip First
School of Physics
Georgia Institute of Technology

Professor John A. Buck
School of Electrical and Computer Engineering
Georgia Institute of Technology

Date Approved: July 09, 2007

This dissertation is dedicated to

all my family

for everything.

ACKNOWLEDGEMENTS

At this moment when I am wrapping up my Ph.D. work, I am so excited and grateful. There have been many people with me throughout the whole journey to my Ph.D. degree. I would like to acknowledge all the individuals for their support and understanding.

First, I want to express my deep gratitude to my Ph.D. advisor, Prof. David S. Citrin, without whose thoughtful advice and full support, this thesis would never be finished. He led me into the wonderful quantum world, and never hesitates to share his insights and knowledge with me. Under his influences, I start to appreciate the involved physics related to nanoscale optoelectronic devices and ultrafast phenomena. His encouragement and long-term vision will accompany me along my continuing investigations in this challenging and enjoyable research field.

I would like to thank Prof. Gee-Kung Chang, Prof. John A. Buck, Prof. Russell D. Dupuis for their time on reading and commenting both of my proposal and dissertation, and Prof. Phillip First for serving on my dissertation committee.

I would like to extend my appreciation to Prof. W. Alan Doolittle and Prof. Abdallah Ougazzaden for fruitful and interesting discussions on solar cells and light emission diodes (LED's), which broadened my view on the optoelectronics area.

I would also like to express my acknowledgement to the present and past members of Nano and Ultrafast Photonics group for their help and friendship. Many thanks to Ms. Janet Myrick for helping me in administrative affairs.

I am also grateful to all my friends in Georgia Institute of Technology. Their companionship makes my Ph.D. study enjoyable.

I want to address my appreciation to my husband Debao Zhou. With his unlimited understanding, support and patience, I am able to get through all difficulties encountered. I cherished the special gift the world brought to us, my little son, Eric. His cute smiles brought me tremendous encouragement and strength.

Finally, I am deeply indebted to my dear parents and younger brother. They gave me everything they could to help me achieve my goal. Specially, they gave up most of their leisure time to help me take care of Eric. No word can express my gratitude to them. This dissertation is dedicated to all my family.

TABLE OF CONTENTS

LIST OF FIGURES

LIST OF ABBREVIATIONS

DP	digitization period
e-e	electron-electron
FIR	far-infrared
FWHM	full width at half maximum
IBSC	intermediate-band solar cell
LO	longitudinal
MBE	molecular beam epitaxy
MIR	mid-infrared
NDR	negative differential resistance
NIR	near-infrared
QC	quantum-cascade
QCL	quantum cascade laser
QW	quantum well
QEP	quadratic eigenvalue problem
QWIP	quantum-well infrared photodetector
SH	second-harmonic
SHG	second-harmonic generation
SML	self-mode-locking
SMS	submonolayer superlattices
SPM	self-phase modulation
SUSYQM	supersymmetric quantum mechanics

TH	third-harmonic
THG	third-harmonic generation

SUMMARY

Nonlinearities in quantum cascade lasers (QCL's) have wide applications in wavelength tunability and ultra-short pulse generation. In this thesis, optical nonlinearities in InGaAs/AlInAs-based mid-infrared (MIR) QCL's with quadruple resonant levels are investigated. Design optimization for the second-harmonic generation (SHG) of the device is presented. Performance characteristics associated with the third-order nonlinearities are also analyzed.

The design optimization for SHG efficiency is obtained utilizing techniques from supersymmetric quantum mechanics (SUSYQM) with both material-dependent effective mass and band nonparabolicity. Current flow and power output of the structure are analyzed by self-consistently solving rate equations for the carriers and photons. Nonunity pumping efficiency from one period of the QCL to the next is taken into account by including all relevant electron-electron (e-e) and longitudinal (LO) phonon scattering mechanisms between the injector/collector and active regions. Two-photon absorption processes are analyzed for the resonant cascading triple levels designed for enhancing SHG. Both sequential and simultaneous two-photon absorption processes are included in the rate-equation model. The current output characteristics for both the original and optimized structures are analyzed and compared. Stronger resonant tunneling in the optimized structure is manifested by enhanced negative differential resistance. Current-dependent linear optical output power is derived based on the steady-state photon populations in the active region. The second-harmonic (SH) power is derived from the Maxwell equations with the phase mismatch included. Due to stronger

coupling between lasing levels, the optimized structure has both higher linear and nonlinear output powers. Phase mismatch effects are significant for both structures leading to a substantial reduction of the linear-to-nonlinear conversion efficiency. The optimized structure can be fabricated through digitally grading the submonolayer alloys by molecular beam epitaxy (MBE).

In addition to the second-order nonlinearity, performance characteristics brought by the third-order nonlinearities are also discussed, which include third-harmonic generation (THG) and intensity dependent (Kerr) refractive index. Linear to third-harmonic (TH) conversion efficiency is evaluated based on the phase-mismatched condition. The enhanced self-mode-locking (SML) effect over a typical three-level laser is predicted, which will stimulate further investigations of pulse duration shortening by structures with multiple harmonic levels.

CHAPTER I

INTRODUCTION

Quantum cascade lasers operate due to population inversion on intersubband transitions in unipolar (i.e., only electron injection) multiple quantum well (QW) structures. They were first realized by J. Faist in F. Capasso's group in 1994 [1], although the general theoretical idea goes back to 1971 [2]. The unique light generation mechanism and carrier transport characteristics make QCL's a type of compact and high-performance laser source in MIR and far-infrared (FIR) regions [3-7]. The large optical nonlineartities associated with intersubband transitions, moreover, make QCL's attractive for tunable light generation in the near-infrared (NIR) to MIR regime, which is of intense interest for gas sensing. Furthermore, the unique combination of giant nonlinearity and ultrafast intersubband carrier dynamics also makes QCL's a good candidate for high-speed MIR optoelectronics. In this chapter, previous studies on nonlinearities of QCL's and their applications are reviewed, which provides a context for the current research objectives. The thesis structure is outlined in the last part of this chapter.

1.1 Overview of Nonlinearities in Quantum Cascade Lasers

1.1.1 Harmonic Generation in Quantum Cascade Lasers

In QCL's, the light is typically generated through intersubband transitions in the conduction band. The intersubband dipole matrix elements (i.e., between different quantum mechanical states of a semiconductor QW structure) are of the order of a few electron-charge nanometers, which are larger by a factor of 10-50 than the corresponding interband transitions [8]. It is for this reason that second-order nonlinearities associated

with intersubband transitions are *giant* compared to those of interband transitions. The theory of second-order susceptibilities based on intersubband processes in asymmetric QW structures was developed by J. Khurgin [9] in the early 1990s. The calculation showed that the second-order susceptibility in the 10-μm range can reach 5×10^{-8} m/V, which is significantly larger than ~$1\text{-}10\times10^{-12}$ m/V for typical bulk nonlinear crystals [10]. The dependence of the second-order susceptibility on band-gap offsets and QW geometries was then investigated. Thus, aside from their linear optical properties, resonant intersubband transitions in coupled QW's can also be designed as strongly nonlinear oscillators, thus providing for giant nonlinear optical susceptibilities [11-14]. For all these designs, the usefulness in nonlinear frequency conversion was limited due to difficulties in efficiently coupling the pump radiation to the intersubband optical transitions. Besides, even with good coupling, there are fundamental problems in the resonant absorption of the external pump radiation and the lack of a suitable phase-matching scheme in most III-V semiconductors. To overcome these difficulties, the monolithic and guided wave approach of integrating the nonlinear optical transitions with the pumping source provides the best solution for efficient coupling. In integrated devices, laser radiation generated by transitions of carriers injected into the active region serves as an intracavity optical pump for the nonlinear frequency converstion. All fields participating in the nonlinear interaction can be at resonance with corresponding intersubband transitions, maximizing the nonlinear optical response. Phase matching or quasi-phase matching can be achieved by selecting optical modes with different transverse order. Such integration was earlier suggested for diode lasers [15].

For QCL's, the nonlinearities can be further enhanced through resonant triple- or quadruple-levels design in the active region with strong second- or third-order nonlinear susceptibilities, resulting in SHG or THG, which makes QCL's attractive sources for multiple-color light emission in the MIR and FIR. The monolithic integration of QCL's with optimized SHG is reported in Ref. [16]. In this design, the QW's in the active region simultanesouly act as the pumping source and medium for nonlinear light generation. The structure is composed of lattice matched GaInAs/AlInAs multiple QW's. The conduction-band diagram and quantized states are shown in Fig. 1.1, where one active region is sandwiched between two injectors. In this design, the active region of the QCL consists of three coupled QW's, which form five quantized energy levels with resonant nonlinear cascades, 2-3-4 for cascade I and 3-4-5 for cascade II. In particular, the band diagram is designed to result in a multi-resonant subband structure so that a subband lies at twice the energy above the lower level of the lasing transition. The fundamental (linear) light emission is at 9.1 μm while that for the SHG emission is at 4.55 μm. Figure 1.2 shows the experimental results; approximately 0.1 W of fundamental peak power results in about 600 nW of SHG light. The linear-to-nonlinear conversion efficiency $h = P_{SHG}/P_{LN}{}^2$ is up to 100 μW/W^2. This QCL design has the clear advantages that it assures a strong overlap and efficient in-plane coupling of fundamental and nonlinear guided modes. Moreover, since the emitted photons produced by the intracavity SHG or THG are at frequencies well below the bandgap, reabsorption is suppressed (though intersubband bound to continuum absorption persists), which is a unique advantage over conventional diode lasers. These features taken together have made SHG in QCL's a very attractive way to access the MIR (3~4 μm) where both

diodes and QCL's have had limited success [17]. This also opens the possibility of compact multicolor MIR sources, which are of intense interest for chemical sensing.

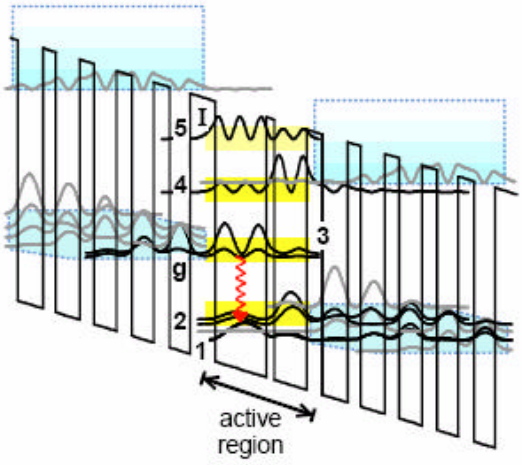

Figure 1.1 Conduction-band diagram for the design in [16] with one active region sandwiched between two injector regions.

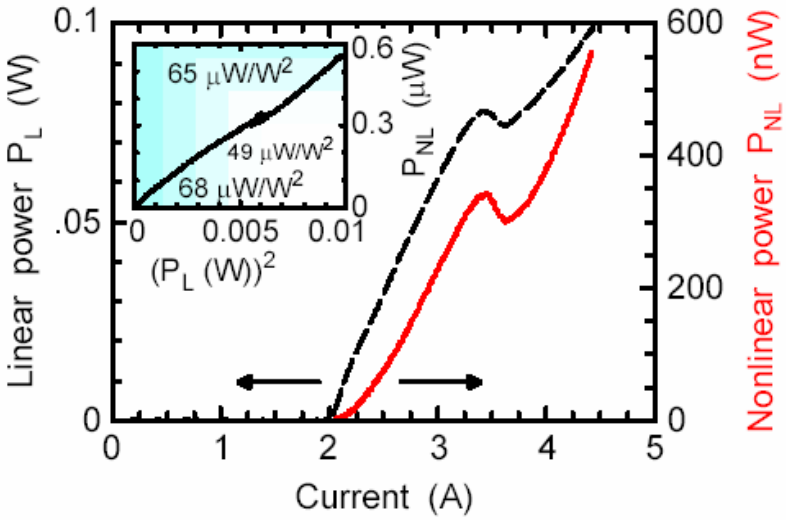

Figure 1.2 Linear (P_L) and nonlinear (P_{NL}) light output versus current.

In this structure, even though some SHG emission is achieved, the linear-to-nonlinear conversion efficiency still has an opportunity to be improved through further design optimization. Also, in [16], it is mentioned that some devices exhibit increased

SHG but no lasing. It would appear there is likely to be competition between gain and the optical nonlinearities through the population distribution among the quantized states within the conduction band. Thus, a comprehensive theoretical model for QCL performance accounting for both linear and nonlinear aspects is worthy to be explored. Some work has been reported on the theoretical modeling of the QCL's [18, 19], but none of these models includes both linear and nonlinear optical processes.

1.1.2 Self-Mode-Locking in Quantum Cascade Lasers

The emission wavelength of QCL's is in typically in the MIR [20-22]. This spectral region is technologically and scientifically important for chemical and biological sensing [23] since many molecules have characteristic absorption features here. One of the advantageous features of QCL's is potentially MIR ultra-short pulse generation. In addition to the large optical nonlinearities associated with intersubband transitions in QCL's, the fast (picosecond) intersubband carrier relaxation controlled by electron-optical phonon scattering is another favorable feature of QCL's. The unique combination of giant optical nonlinearities and ulfrafast dynamics makes QCL's attractive in applications involving high-speed optoelectronic devices. Generation of picosecond pulses by SML in QCL's has been reported in [24]. The origin of SML was interpreted as due to a new kind of Kerr lensing mechanism in which the refractive index is dependent on the lasing intensity of the medium associated with intersubband transitions. The intensity-dependent refractive index (Kerr nonlinearity) of the lasing transition creates a nonlinear waveguide where the optical losses decrease with increasing intensity. This favors the generation of ultrashort pulses because of their instantaneous intensity relative to continuous-wave emission. Later on, the observation of stable pulse emission in self-

mode locked QCL's was reported in [25]. The measurement was taken by direct down-converting the detector signal by heterodyning with an RF signal A pulse duration of ~12 ps was estimated from the measured increase of the SHG signal in pulsed emission compared to the power expected from the SHG signal in CW emission. These experiments coupled with theoretical modeling strongly indicate that SML in QCL's is a feasible technique to achieve stable picosecond pulses with high peak intensity. So far, all the structures studied for SML in QCL's are three-level intersubband devices with one pair of radiative transition levels; thus, only single-photon process dominates the optical transition. As we discuss later, QCL's with additional harmonic transition levels may significantly enhance the Kerr nonlinearity.

1.2 Motivation

Based on the overview above of the current state of the art, our research has focused on improving and understanding QCL nonlinearities for different scenarios by means of theoretical exploration. A systematic optimization approach will be proposed below to enhance SHG in QCL's. In order to evaluate both the linear and nonlinear performances of QCL's, a theoretical model including carrier transport and wave propagation was built. Nonunity pumping efficiency from one period of the QCL to the next was taken into account by including all relevant e-e and LO phonon scattering mechanisms between the injector/collector and active regions. Compared to existed modeling schemes of QCL's, significance of the model lies in the incorporation of two-photon processes into carrier dynamics analysis, which are important for both linear and nonlinear performance of optoelectronic devices with SH or TH resonant levels. In addition, our investigations

extend to third-order nonlinearities, which lead to both THG and enhanced nonlinear refractive index. The research is discussed in detail in the following section.

1.2.1 Optimization of Quantum Cascade Lasers with Second-Harmonic Generation

Efficient intracavity SHG can be achieved in QCL's with strong second-order nonlinear susceptibility $c^{(2)}$. Room for improvement is likely to exist by judicious design of the band profile. Moreover, a simple understanding of SHG and QCL operation would indicate that SHG and modal gain must be traded off since the electron population distribution favorable to one would appear to be unfavorable to the other. The purpose of this part of our research is to design QCL's for optimized SHG and at the same time with improved modal gain.

The optimization scheme is initiated from the figure of merit for SHG, i.e., $c^{(2)}$,

$$c^{(2)}(2w) \propto \frac{M_{ij} M_{jk} M_{ik}}{(E_{ki} - 2\hbar w - ig_{ki})(E_{ji} - \hbar w - ig_{ji})}, \tag{1.1}$$

where M_{ij} is the dipole matrix element between levels i and j, E_{ij} is energy separation between levels i and j, and and $2g_{ij}$ is the full width at half maximum (FWHM) of the transition broadening between levels i and j.

From Eq. (1.1), it can be seen that $c^{(2)}$ is proportional to the dipole matrix element product $M_{23}M_{34}M_{24}$ for cascade I and $M_{34}M_{45}M_{35}$ for cascade II. The nonlinearity can be further enhanced by increasing the dipole matrix element products while retaining the multiple resonances between levels. The method is based on SUSYQM, where the energy potential profile is varied in an isospectral manner with dependency on a single parameter. SUSYQM has been employed in the gain maximization in QCL's in [26] and optimization of resonant second-order nonlinear

susceptibility $c^{(2)}$ for the harmonic oscillator in [27]. The current work generalizes this method to the enhancement of SHG in QCL's and applies it to material systems with larger conduction-band offsets by accounting for the energy-dependence of the effective mass.

1.2.2 Third-Order Nonlinearities in Quantum Cascade Lasers

In the bandstructure of the active region of the QCL structure of [16], there are five energy levels, E_1, E_2, E_3, E_4, and E_5, of which E_1 is the ground state, and E_2, E_3, E_4, and E_5 are equally spaced with energy intervals resonant with the lasing photon energy $\hbar w$. The THG resonant cascade $E_2 - E_3 - E_4 - E_5$ consists of two SHG resonant triplets $E_2 - E_3 - E_4$ and $E_3 - E_4 - E_5$.

Even though the structure was originally designed for optimized SHG, there are additional optical nonlinearities related to the tetrad of resonant levels. We start our discussion with the third-order contribution to the nonlinear polarization,

$$\tilde{P}^{(3)}(t) = \chi^{(3)}\tilde{E}(t)^3, \tag{1.2}$$

where $\tilde{E}(t)$ is the applied electric field given by

$$\tilde{E}(t) = E\cos(wt). \tag{1.3}$$

With the substitution of Eq. (1.3), Eq. (1.2) is expanded as

$$\tilde{P}^{(3)}(t) = \frac{1}{4}c^{(3)}(3w;w,w,w)E^3\cos(3wt) + \frac{3}{4}c^{(3)}(w;w,-w,w)E^3\cos(wt). \tag{1.4}$$

The first term in Eq. (1.4) describes a response at frequency $3w$ that is due to an applied field at frequency w. This term leads to THG. The second term describes a nonlinear contribution to the polarization at the frequency w of the incident field. This term leads to a nonlinear contribution to the refractive index at frequency w and thus

results in SML of QCL's. Studies will come to the conclusion about the effect of multiple harmonic resonance levels on the Kerr effect of QCL's and point out a possible way of shortening the emission pulse through band structure design of lasing medium.

1.3 Thesis Outline

The rest of this thesis includes the following parts:

Chapter 2 reviews the theoretical background of QCL electronic structure, operation principle, carrier scattering mechanisms, and the nonlinear aspects of QCL's. Electronic and optical transitions in QCL's occur between quantized states in the conduction band, which offers unique design flexibility compared to conventional diode lasers. The carrier transport is fully dependent on the bandstructure and constituent materials as well as the operation environment. Scattering mechanisms, such as e-e and phonon scattering result in the desired performance for numerous applications in the MIR .

Chapter 3 describes the procedure to optimize QCL's with respect to the resonant second-order nonlinearity, based on the SUSYQM approach. After that, carrier transport and the power output of the structure are analyzed by self-consistently solving rate equations for the carriers and photons. The current-dependent linear optical output power is derived based on the steady-state photon populations in the active region. The SH power is obtained from the Maxwell equations with the phase mismatch included. The optimized structure can be fabricated through digitally grading the submonolayer alloys by molecular beam epitaxy (MBE) technique.

Chapter 4 presents the study on MIR QCL's with a pair of triply harmonic resonant levels. Potential applications of such designs are discussed based on the resonant

third-order nonlinear susceptiblility at the TH frequency and that at fundamental frequency. The TH power generated is evaluated based on the nonlinearity susceptibility, mode overlap with the mode at fundamental frequency, and the effect of phase mismatch. The higher-order TH mode with the best phase-matching to the fundamental mode is identified, which greatly improves the linear to TH conversion efficiency. In addition to single-photon processes, resonant two-photon processes are included in the evaluation of third-order nonlinearity, which results in the enhancement of the positive nonlinear refractive index leading to SML mechanism.

The conclusions are summarized in Chapter 5.

CHAPTER 2

THEORETICAL BACKGROUND

Design of QCL's with enhanced nonlinearity is based on theories of optical transitions in MIR QCL's and nonlinear optics. While most of the concepts are quite general, the focus is on the GaInAs/AlInAs material system [16].

2.1 Electronic States in Semiconductor Heterostructures

Intersubband lasers are made possible by the growth of multiple heterostructures, which are atomically abrupt layers composed of materials with different bandgaps, i.e., GaInAs/AlInAs material system. Thus there is a sharp discontinuity in the band diagrams at the heterojuction between two such materials. When the layers are made thin enough, i.e., on the order of a DeBroglie wavelength, electron motion is restricted in the growth direction $\hat{x}$ and its energy is quantized.

In the treatment, effective-mass theory [28] in the envelope-function approximation is used to obtain the electronic wavefunctions and quantized energy levels. The Γ-point effective mass is used to describe the conduction-band curvature ($m^* = 0.041m_0$ in InGaAs). The time-independent Schrödinger equation with the effective-mass theory is given as

$$\left[\frac{\hbar^2}{2m^*}\nabla^2 + E(\mathbf{r})\right]? (\mathbf{r}) = E? (\mathbf{r}), \tag{2.1}$$

where the wavefunction $? (\mathbf{r})$ for the electron is given by

$$? (\mathbf{r}) = F(\mathbf{r})U_{n,0}(\mathbf{r}), \tag{2.2}$$

where $U_{n,0}(\mathbf{r})$ is the Bloch state wavefunction at the band minimum and $F(\mathbf{r})$ is the envelope function and satisfies the effective-mass equation. The various materials are represented by the spatially dependent effective mass $m^*(x)$ and the potential $E_c(x)$ corresponds to relative conduction-band offset including the externally applied electric field. The effective-mass equation then becomes

$$\left[-\frac{\hbar^2\nabla_{//}^2}{m^*(x)}-\frac{\hbar^2\partial}{2\partial x}\frac{1}{m^*(x)}\frac{\partial}{\partial x}+E_c(x)\right]F(\mathbf{r})=EF(\mathbf{r}). \tag{2.3}$$

where $\nabla_{//}$ is the in-plane (*yz* plane) differential operator [29]. The solution for the envelope function is given by

$$F(\mathbf{r})=\frac{1}{\sqrt{S_{//}}}e^{i\mathbf{k}_{//}\cdot\mathbf{r}_{//}}y_n(\mathbf{k}_{//},x) \tag{2.4}$$

where $y_n(\mathbf{k}_{//},x)$ satisfies

$$\left[-\frac{\hbar^2 d}{2dx}\frac{1}{m^*(x)}\frac{d}{dx}+E_c(x)+\frac{\hbar^2\mathbf{k}_{//}^2}{2m^*(x)}\right]y_n(\mathbf{k}_{//},x)=E_n(\mathbf{k}_{//})y_n(\mathbf{k}_{//},x), \tag{2.5}$$

and $\mathbf{k}_{//}$ is the in-plane wavevector, *n* is the subband index, and $S_{//}$ is the normalization area. The spatially dependent effective mass introduces a coupling between the in-plane and *x* directions. The coupling is usually neglected and Eq. (2.5) becomes the one-dimensional Schrödinger equation [29].

$$\left[-\frac{\hbar^2 d}{2dx}\frac{1}{m^*(x)}\frac{d}{dx}+E_c(x)\right]y_n(x)=E_n y_n(x), \tag{2.6}$$

where the energy is given by

$$E_n(\mathbf{k}_{//})=E_n+\frac{\hbar^2 k_{//}^2}{2m^*}, \tag{2.7}$$

with m^* the effective mass of the well material. Equation (2.7) is the sum of the quantized energy in the x-direction and the in-plane free particle kinetic energy. Equation (2.7) means the in-plane/x-direction coupling is neglected, which is seen to be justified by considering that the inclusion of this coupling in Eq. (2.6) would effectively change the barrier height $E_c(x)$ by the energy

$$E_D = \frac{\hbar^2 k_{//}^2}{2m^*}\left(\frac{m^*}{m^*(x)} - 1\right), \tag{2.8}$$

which can be derived from the comparison between Eqs. (2.5) and (2.6). Under the condition that the in-plane kinetic energy is modest compared to the barrier height (520 meV for the InGaAs/AlInAs system), and the barrier and well effective mass do not differ too much, it is reasonable to neglect this coupling. Although the states calculated are typically assumed to be discrete stationary states, this is not strictly true. Under the application of an electric field, the states acquire a finite lifetime due to field ionization, i.e., they may escape into the continuum. Escape to continuum is accounted for via an escape time, and is usually much longer than intersubband scattering times.

The parabolic E-k dispersion relationship in Eq. (2.7) is accurate only at energies close to the conduction-band minimum (typically, no further 200 meV from this minimum) [30]. For the structure studied in this thesis, band nonparabolicity should be included due to the large conduction-band offset (520 meV) at the InGaAs/AlInAs heterojunction. The nonparabolicity is modeled by an energy-dependent effective mass [31], which is expressed as

$$m_{np}^*(x,E) = m^*\left(1 + \frac{2gm^*(x)\times(E - E_{cbm})}{\hbar^2}\right), \tag{2.9}$$

where $m^*(x)$ is the conduction-band effective mass for the bulk well or barrier materials, respectively and g is the nonparabolicity coefficient with unit m^2. In the current model, g is assumed to be the same for the barrier and well materials. With the addition of band nonparabolicity, Eq. (2.6) is modified as,

$$\left[-\frac{\hbar^2 d}{2dx}\frac{1}{m^*_{np}(x,E)}\frac{d}{dx}+E_c(x)\right]y_n(x)=E_n y_n(x). \tag{2.10}$$

where the effective mass $m^*_{np}(x,E)$ is both spatially and energy dependent.

The population in the electronic states introduces space charges which consequently affect the conduction-band profile $E_c(x)$, i.e., band bending. For this reason, sometimes it is necessary to solve the Poisson equation [29]

$$\frac{d}{dx}\left[e(x)\frac{d}{dx}\mathrm{F(x)}\right]=-r(x), \tag{2.11}$$

where F(x) is the electrostatic potential, $e(x)$ is the spatially varying permittivity, and $r(x)$ is the charge density. This is equivalent to the Hartree approximation. The potential energy in Eqs. (2.3), (2.5), and (2.6) is

$$E_c(x)=E_{c,0}(x)-e\Phi(x), \tag{2.12}$$

where $E_{c,0}(x)$ is the conduction-band offset between intrinsic materials composing the heterostructure. The Poisson and Schrödinger equations are iteratively solved to arrive at a self-consistent solution of the Schrödinger equation. However, for the structure discussed in this thesis, the electron doping density is sufficiently low that $E_c(x)$ itself is not significantly perturbed, and no self-consistent solution is necessary.

2.2 Operation Principles of Quantum Cascade Lasers

In QCL's, the optical transition occurs between quasi-discrete energy states within the conduction band. These states arise from the quantization of electron motion in the active region's nanometer-thick layers [32]. By adjusting the width and shape of the QW's, one can design an energy-level difference that leads to a desired emitted wavelength. An electron remains in the conduction band after emitting a laser photon. The electron can therefore be recycled by being injected into an adjacent identical active region, where it emits another photon, and so forth. To achieve this cascading emission of photons, active regions are alternated with doped electron injectors and an appropriate bias voltage is applied. The active region-injector stages of the QCL give rise to an energy staircase in which photons are emitted at each of the steps. The number of stages typically ranges from 20 to 50 for lasers designed to emit in the 4-8 μm range [33]. The cascade effect is responsible for the very high powers that QCL's can attain. Figure 2.1 illustrates the band diagram of a QCL, where the laser transition is symbolized by the red wavy arrows. Under the electric field applied across the laser, electrons are injected from the miniband's ground state *g* into the upper state of the laser transition—level 3 of the active region. The thinnest QW in the active region enhances tunneling of the electrons from the injector into the upper state. Stimulated photon emission occurs on the lasing transition 3-2. For laser action to occur, the electron population in stage 3 must exceed that of state 2. This population inversion is achieved if the relaxation time t_{32} for the transition from state 3 to state 2 exceeds the electron's lifetime t_2 in state 2. To maximize the population inversion, the energy separation between state 2 and 1 is designed to be equal to the LO phonon energy, which is 34 meV for InGaAs. In this way, electrons in state 2

will quickly scatter into state 1 because of the resonant nature of the transition. Hence, population inversion in QCL is maintained by careful design of the electron transport time and the phonon scattering time between intersubband transitions. According to Vasko and Kuznetsov [34], for QW structures, the dimensionless relative gain (negative of absorption) per layer x_w is adopted to characterize the emission of optical power by radiative intersubband transition. The following analysis on the gain proves the relationship between lasing and population inversion mentioned above.

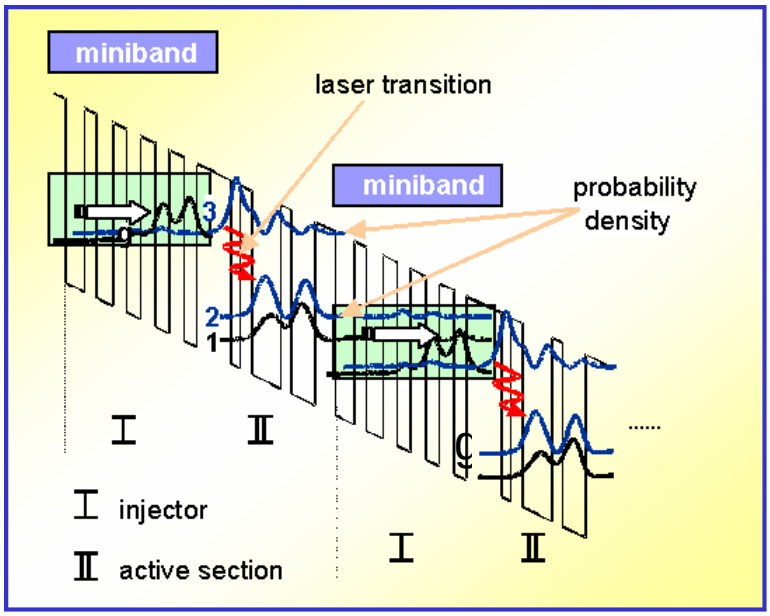

Figure 2.1 Two periods of a typical quantum cascade laser structure.

Since the lasing levels are sufficiently low (within 200 meV of the conduction-band minimum of the well material), the band nonparabolicity for analyzing the gain can be ignored, thus the lasing subbands have the same curvature, and hence the joint density of states for an intersubband transition is a Dirac δ-function at the subband separation $\hbar w = E_3 - E_2$. The relative gain is expressed as,

$$x = \frac{(2pe)^2}{wc\sqrt{e}L^2} M_{32}^2 d(E_3 - E_2 - \hbar w) \sum_{k_\perp} [f_3(k_\perp) - f_2(k_\perp)] \tag{2.13}$$

where L^2 is the normalization area of QW, M_{32} is the dipole matrix element between lasing states 3 and 2, and $f_{3(2)}(k_\perp)$ is the Fermi-distribution function at in-plane momentum $k_\perp$.

The population inversion between the lasing states is

$$DN = N_3 - N_2 = r_c^{2D} \sum_{k_\perp} [f_3(k_\perp) - f_2(k_\perp)] \Big/ L_P \,, \tag{2.14}$$

with $r_c^{2D} = \frac{m_e}{p\hbar^2}$ the 2D density of states in conduction subbands and L_P the thickness of one period of QCL. By combining Eqs. (2.13) and (2.14), the relative gain can be expressed in terms of population inversion as

$$x = \frac{4e^2 p^3 \hbar^2}{m_c wc\sqrt{e}} L_P \left| \langle 3 | \mathrm{e} \cdot \hat{\mathrm{v}} | 2 \rangle \right|^2 d(E_3 - E_2 - \hbar w) \Delta N \,. \tag{2.15}$$

The δ-function can be approximated as a Lorentzian,

$$d(E_f - E_i + \hbar w) \approx \frac{1}{p} \frac{g_{32}}{(E_3 - E_2 - \hbar w)^2 + g_{32}^2}, \tag{2.16}$$

where $2g_{32}$ is the FWHM of the 3→2 transition. With the substitution of Eq. (2.15), Eq (2.16) can be rewritten as

$$x = \frac{4e^2 p^2 \hbar^2}{m_c wc\sqrt{e}} L_P z_{32}^2 \Delta N \frac{g_{32}}{(E_3 - E_2 - \hbar w)^2 + g_{32}^2} \,. \tag{2.17}$$

For QCL's, it is more convenient to use modal gain G_m as a figure of merit of the design. Modal gain is simply the gain per unit thickness, i.e.,

$$G_m = \frac{x}{L_P} = \frac{4e^2 p^2 \hbar^2 M_{32}^2 DN g_{32}}{m_c wc\sqrt{e}[(E_3 - E_2 - \hbar w)^2 + g_{32}^2]}. \quad (2.18)$$

It can be seen from the above derivation that population inversion is a key factor that influences the modal gain of QCL's. The population inversion is dependent on the lifetime of the lasing states as well as the electron scattering rate between them [33],

$$DN \propto t_3 (1 - \frac{t_2}{t_{32}}). \quad (2.19)$$

2.3 Carrier Scattering Dynamics of Quantum Cascade Lasers

In quantum cascade (QC) structures, the design of energy levels and wavefunctions allows scattering rates to be engineered to provide a population inversion. A proper understanding of inter- (and intra-) subband scattering is essential for the design and understanding of QCL's. The important intersubband scattering channels are displayed in Fig. 2.2. It has been well established that LO phonon scattering is the dominant intersubband scattering mechanism for subband separations greater than the LO-phonon energy E_{LO} [35, 36]. For intersubband transitions where the separation is less than E_{LO}, emission of LO-phonons is energetically forbidden at low temperatures. Nonradiative relaxation is therefore dominated by a combination of e-e scattering, electron-impurity scattering, and LO-phonon scattering of the high energy tail of the subband electron distribution. Since we assume the material has low impurities, impurity scattering is not taken into consideration in the current research.

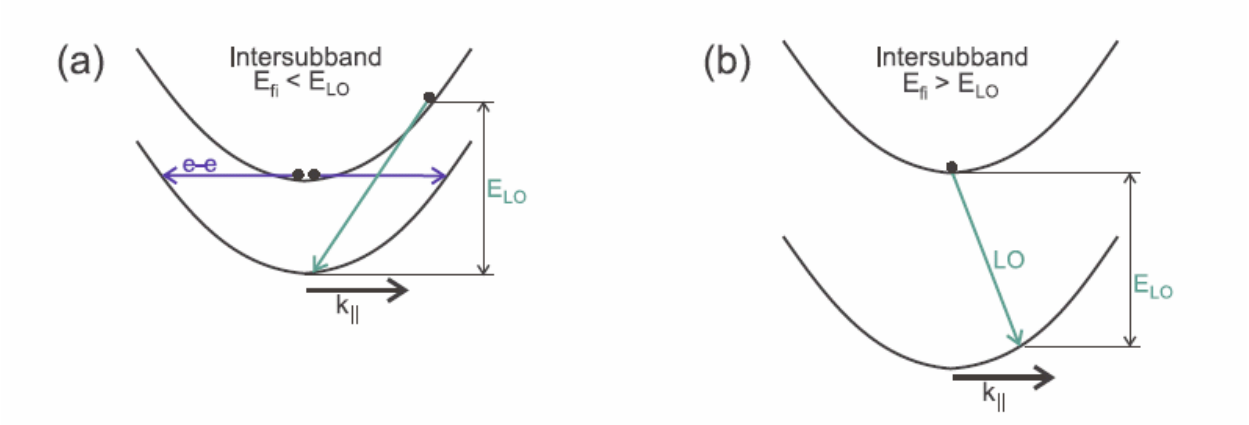

Figure 2.2 Important intersubband scattering mechanisms : (a) $E_{fi} < E_{LO}$ and (b) $E_{fi} > E_{LO}$.

Intrasubband transitions are important process in cooling the subband electron gas [37]. The effect of intrasubband e-e scattering is to thermalize the electron distribution inside a particular subband. In the present calculation, intrasubband scattering is ignored and the electrons in each subband are assumed to be thermalized to the same effective temperature, which may be the same as the lattice temperature. The electron population in each subband can be described by quasi-Fermi distribution [38].

Without concerning ourselves here with intrasubband transitions, among all the intersubband transition mechanisms, the dominant ones are LO phonon scattering and e-e scattering. Thus, the preliminary study is focused on these two scattering processes.

2.3.1 Longitudinal Phonon Scattering

The formalism used for LO phonon scattering is based on that of Smet *et al.*[39]. The total scattering rate for absorption of LO-phonons for initial state $\left|i,\vec{\mathbf{k}}_i\right\rangle$ can be written as

$$W_{i\to f}^{em}(\vec{k}_i) = \frac{m^* e^2 w_{LO}}{2\hbar^2}\left(\frac{1}{e_\infty} - \frac{1}{e_s}\right)(n_{wLO}+1)\int_0^{2p} B_{i\to f}(q_\perp)dq \,, \qquad (2.20)$$

where n_{wLO} is the Bose-Einstein distribution for the phonons [28], e_s and e_∞ are the static and high frequency dielectric constants, and $\hbar w_{LO}$ is the LO-phonon energy. The expression for $B_{i\to f}$ is

$$B_{i\to f}(q_\perp) = \int_{-\infty}^{\infty} dx \int_{-\infty}^{\infty} dz' \, y_f^*(x) y_i(x) y_i^*(x') y_f(x') I(x, x', q_\perp). \tag{2.21}$$

The envelope functions $y_{i,f}(x)$ for the initial or final subband can be obtained through solving Schrödinger's equation. $I(z, z', q_\perp)$ is expressed as

$$I(x, x', q_\perp) = \left[\frac{1}{(q_\perp^2 + q_s^2)^{\frac{1}{2}}} - \frac{|z - z'| q_s^2/2}{(q_\perp^2 + q_s^2)} - \frac{q_s^2/2}{(q_\perp^2 + q_s^2)^{3/2}} \right] \exp[-\sqrt{q_\perp^2 + q_s^2}\,|x - x'|], \tag{2.22}$$

where $q_\perp$ is the in-plane momentum, and q_s is inverse screening length, which accounts for the screening of e-e interactions involving in the electron-LO phonon scattering process. The screening becomes significant when the electron density increases above 10^{11} cm^{-2} [40].

In Eq. (2.20), q is the angle between the initial and final states characterized by wave-vectors $\vec{\mathbf{k}}_i$ and $\vec{\mathbf{k}}_f$, and thus the q-integration corresponds to the integration over all possible final states. The exchanged in-plane momentum $q_\perp$ can be expressed using the momentum conservation equation

$$q_\perp^2 = \left| \vec{\mathbf{k}}_i - \vec{\mathbf{k}}_f \right|^2 = k_i^2 + k_f^2 - 2k_i k_f \cos q. \tag{2.23}$$

The magnitude of the in-plane momentum of final states can be decided from energy conservation

$$k_f^2 = k_i^2 + \frac{2m^*(E_f - E_i + \hbar w_{LO})}{\hbar^2}. \tag{2.24}$$

The total scattering time between subbands $t_{i\to f}$ can then be obtained by averaging over all possible initial states in the subband:

$$\frac{1}{t_{i\to f}} = \frac{\int_0^\infty dE_k \, r_c^{2D}(E_k) f_i(E_k) W_{i\to f}^{em}(E_k)}{\int_0^\infty dE_k \, r_c^{2D}(E_k) f_i(E_k)}. \tag{2.25}$$

The quasi-Fermi distribution of the initial state contributes significantly to the average scattering time. It will change with the population at the subband. In the initial calculation, it is assumed that the population in the lower subband is zero.

Figure 2.3 illustrates our calculation results on the average LO phonon scattering rate under different energy separations. The population density of electrons here is 10^{10} cm^{-2}. Since screening is not significant at this low carrier concentration, it is ignored in the current calculation. Our results agree well with the results in [41]. The peak scattering rate coincides with the LO phonon energy, which is called resonant LO phonon scattering. The intersubband transition in this case is vertical. When the energy separation is greater than the LO phonon energy, electrons in higher subbands have sufficient energy to emit an LO phonon and scatter to the lower subband. The transition is diagonal in *k*-space, that is, it is accompanied by momentum transfer between the electron and the phonon. It is shown in the plot that the scattering rate is inversely dependent on the energy separation as well as in-plane momentum transfer, which can also be read from Eq. (2.22). When the separation between subband minima is less than the LO phonon energy, electrons in the high-energy tail of the upper subband can contribute to the emitted phonons. In this region (left part of plot), the scattering rate decreases when the energy separation becomes smaller since electrons in higher energy tail have to be

involved in the scattering, and their population is small according to the quasi-Fermi distribution in the subband.

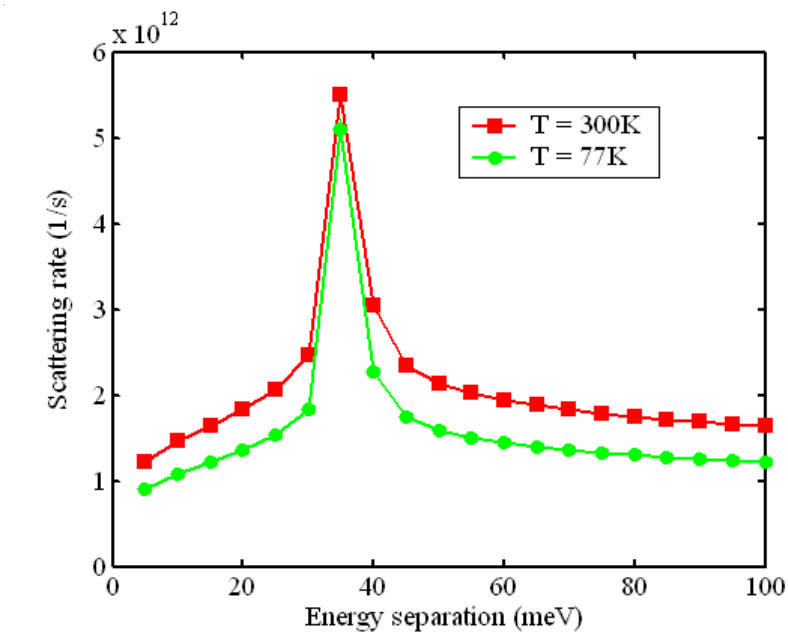

Figure 2.3 The average longitudinal phonon scattering rate as a function of subband energy separation.

2.3.2 Electron-Electron Scattering

Electron-electron scattering is the second most important scattering mechanism in determining intersubband optical properties. In this mechanism, two initial states (i, j) and two final states (f, g) are involved. Thus in a two-subband system, there are three ways in which electron can scatter from the upper to lower level. They are illustrated in Fig. 2.4.

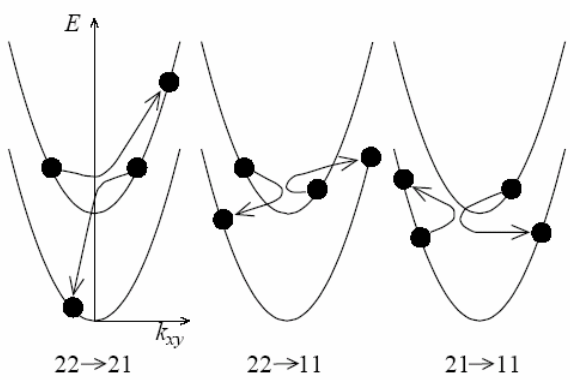

Figure 2.4 The three different intersubband electron-electron scattering mechanisms .

The total scattering out of the initial electron state $\left|i,\vec{\mathbf{k}}_i\right\rangle$ is [39],

$$W_{i,j\to f,g}(k_i)=\frac{e^4}{2p\hbar e_r^2 e_0^2}\int d^2\vec{k}_j\int d^2\vec{k}_f\int d^2\vec{k}_g\,\frac{\left|A_{i,j\to f,g}(q_\perp)\right|^2}{e_{sc}^2(q_\perp,T)q_\perp^2}\,f_j(\vec{k}_j)(1-f_f(\vec{k}_f))(1-f_g(\vec{k}_g))$$
$$\times d(E_f(\vec{k}_f)+E_g(\vec{k}_g)-E_i(\vec{k}_i)-E_j(\vec{k}_j))\times d(\vec{k}_f+\vec{k}_g-\vec{k}_i-\vec{k}_j) \tag{2.26}$$

where

$$q_\perp=\left|k_i-k_f\right|, \tag{2.27}$$

and

$$A_{i,j\to f,g}(q_\perp)=\int_{-\infty}^{\infty}dx\int_{-\infty}^{\infty}dx'\,y_i(x)y_f^*(x)y_j(x')y_g^*(x')e^{-q_\perp|x-x'|}. \tag{2.28}$$

The term e_{sc} is the correction to the permittivity due to screening. The carrier distribution functions $f_f(\vec{k}_f)$ and $f_g(\vec{k}_g)$ were included to properly account for state blocking. The two d -functions represent the energy and in-plane momentum conservation, respectively. They simplify the $\vec{k}_f$ and $\vec{k}_g$ integrations, i.e., $\vec{k}_f$ and $\vec{k}_g$ can be represented in terms of $\vec{k}_i$ and $\vec{k}_j$. For convenience, the following definitions are made,

$$\vec{k}_{ij}=\vec{k}_j-\vec{k}_i, \tag{2.29a}$$

$$\vec{k}_{fg} = \vec{k}_g - \vec{k}_f . \tag{2.29b}$$

Let the gap between the subband edges be ΔE . Due to energy conservation,

$$k_f^2 + k_g^2 = k_i^2 + k_j^2 + \frac{4m_e}{\hbar^2}\Delta E . \tag{2.30}$$

From in-plane momentum conservation, we have

$$\left|\vec{k}_i + \vec{k}_j\right| = \left|\vec{k}_f + \vec{k}_g\right|. \tag{2.31}$$

Equations (2.30) and (2.31) then give

$$\left|\vec{k}_{fg}\right|^2 = \left|\vec{k}_{ij}\right|^2 + \frac{8m_e DE}{\hbar^2} . \tag{2.32}$$

By making use of momentum conservation and Eq. (2.32), the momentum $q_\perp$ can finally be rewritten as

$$q_\perp(k_i, k_j) = \frac{\left|\vec{\mathrm{k}}_{ij} - \vec{\mathrm{k}}_{fg}\right|}{2} = \frac{\sqrt{2k_{ij}^2 + \frac{8m_e\Delta E}{\hbar^2} - 2k_{ij}\sqrt{k_{ij}^2 + + \frac{8m_e\Delta E}{\hbar^2}\cos f}}}{2}, \tag{2.33}$$

where f is the angle between $\vec{k}_{ij}$ and $\vec{k}_{fg}$.

For a given initial electron in-plane momentum $\vec{k}_i$, $\vec{k}_j$ can be written as $\left|\vec{k}_j\right|\angle q$ with q the angle between $\vec{k}_i$ and $\vec{k}_j$. The in-plane momentum of the final states can be derived according to the vectors relationships shown in Fig. 2.5.

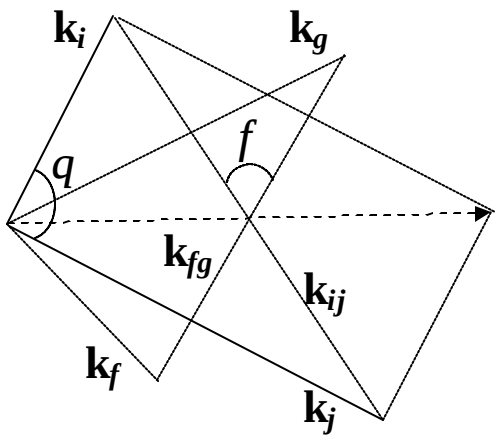

Figure 2.5 Vector scheme for initial and final momenta.

With the expression of $\vec{k}_f$ and $\vec{k}_g$ plugged into the carrier distribution functions $f_f(\vec{\mathbf{k}}_f)$ and $f_g(\vec{\mathbf{k}}_g)$, the *d*-function then permits reduction of multiple integral (2.26) to

$$W_{i,j\to f,g}(k_i) = \frac{e^4 m_e}{p\hbar^3 e_r^2 e_0^2} \int_0^p df \int d^2 k_j \int_0^{2p} dq \int \frac{\left|A_{i,j\to f,g}(q_{\perp})\right|^2}{e_{sc}^2(q_\perp, T) q_\perp^2} F(k_i, k_j, q, f), \qquad (2.34)$$

where all the probabilities of population factors are lumped into $F(k_i, k_j, q, f)$.

Obviously, as seen in Fig. 2.4, the process 2, 2' 1, 1 is the most efficient transition, in which the two electrons in the upper subband scatter into lower subband. Figure 2.6 plots the result on the average e-e scattering rate with such mechanism, which agrees with the result in [41], The form of this curve is much simpler than that of the LO phonon scattering rate. The scattering rate monotonically decreases as the subband separation increases.

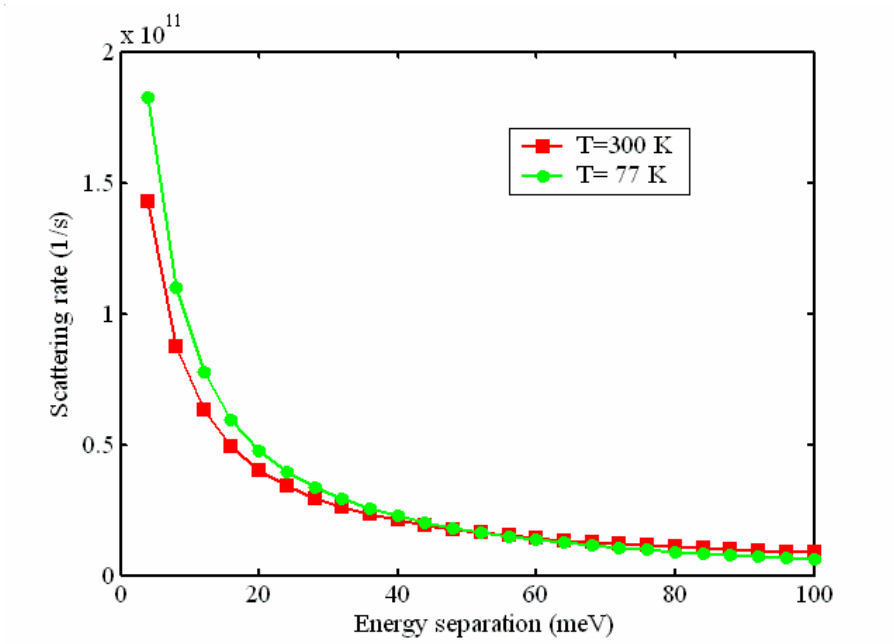

Figure 2.6 The average 22-11 electron-electron scattering rate as a function of subband energy separation.

2.4 Optical Nonlinearities and Harmonic Generation

Nonlinear optical phenomena occur when the response of material system to an applied optical field depends in a nonlinear manner upon the strength of the optical field [42]. In linear optics, the induced polarization depends linearly upon the electric field; this can be described by

$$\tilde{P}(t) = c^{(1)}\tilde{E}(t), \tag{2.35}$$

where the constant of proportionality $c^{(1)}$ is known as the linear susceptibility. In nonlinear optics, the optical response can often be described by generalizing Eq. (2.35) by expressing the polarization $\tilde{P}(t)$ as a power series in the field strength $\tilde{E}(t)$ as

$$\tilde{P}(t) = c^{(1)}\tilde{E}(t) + c^{(2)}\tilde{E}^2(t) + c^{(3)}\tilde{E}^3(t) + \cdots \equiv \tilde{P}^{(1)}(t) + \tilde{P}^{(2)}(t) + \tilde{P}^{(3)}(t) + \cdots . \tag{2.36}$$

The quantities $c^{(2)}$ and $c^{(3)}$ are known as the second-order and third-order nonlinear optical susceptibilities.

2.4.1 Second-Order and Third-Order Polarizations

Suppose the electric-field strength of a monochromatic laser beam is

$$\tilde{E}(t) = E\cos(\omega t), \tag{2.37}$$

The second-order polarization is related to the electric field through second-order nonlinear susceptibility $\chi^{(2)}$ as,

$$\tilde{P}^{(2)}(t) = \chi^{(2)}\tilde{E}(t)^2 = \frac{1}{2}\chi^{(2)}E^2\cos(2\omega t) + \frac{1}{2}\chi^{(2)}E^2. \tag{2.38}$$

The second-order polarization consists of a contribution at zero frequency and a contribution at 2ω. The 2ω contribution leads to the generation of radiation at the SH frequency. SHG can also be thought as the interaction of photons at various frequency components of the field, i.e., two photons of frequency ω are destroyed and a photon of frequency 2ω is simultaneously created in a single quantum-mechanical process.

The third-order polarization is related to the electric field through the third-order nonlinear susceptiblity $\chi^{(3)}$ as,

$$\tilde{P}^{(3)}(t) = \chi^{(3)}\tilde{E}(t)^3 = \frac{1}{4}\chi^{(3)}E^3\cos(3\omega t) + \frac{3}{4}\chi^{(3)}E^3\cos(\omega t). \tag{2.39}$$

The first term in the right side of Eq. (2.39) describes a response at frequency $3w$ that is due to an applied field at frequency w. This term leads to THG. The second term in Eq. (2.39) describes a nonlinear contribution to the polarization at the frequency w of the incident field. This term leads to a nonlinear contribution to the refractive index at frequency w and thus results in SML. The following section describes the derivation of the relationship between the nonlinear refractive index and $\chi^{(3)}$.

2.4.2 Nonlinear Refractive Index

Equation (2.39) above can be rewritten more clearly as,

$$\tilde{P}^{(3)}(t) = \frac{1}{4}\chi^{(3)}(3\omega;\omega,\omega,\omega)E^3\cos(3\omega t) + \frac{3}{4}\chi^{(3)}(\omega;\omega,\omega,-\omega)E^3\cos(\omega t)\,. \qquad (2.40)$$

The total polarization up to the third-order in responding to the applied electric field is as follows,

$$\tilde{P}(t) = \tilde{P}^{(1)}(t) + \tilde{P}^{(2)}(t) + \tilde{P}^{(3)}(t)\,, \qquad (2.41)$$

in which

$$\tilde{P}^{(1)}(t) = \chi^{(1)}\tilde{E}(t) = \chi^{(1)}E\cos(\omega t)\,. \qquad (2.42)$$

Inserting Eqs (2.42), (2.38), (2.39) into Eq. (2.41), Eq. (2.41) can be expanded as,

$$\begin{aligned}\tilde{P}(t) &= \chi^{(1)}E\cos(\omega t) + \frac{1}{2}\chi^{(2)}E^2\cos(2\omega t) + \frac{1}{2}\chi^{(2)}E^2 + \frac{1}{4}\chi^{(3)}E^3\cos(3\omega t) + \frac{3}{4}\chi^{(3)}E^3\cos(\omega t)\\ &= \frac{1}{4}\chi^{(3)}E^3\cos(3\omega t) + \frac{1}{2}\chi^{(2)}E^2\cos(2\omega t) + \left[\chi^{(1)}E + \frac{3}{4}\chi^{(3)}E^3\right]\cos(\omega t) + \frac{1}{2}\chi^{(2)}E^2\end{aligned} \qquad (2.43)$$

from which, it can be seen that third term is related to polarization at the incident field frequency ω, it can be rewritten as,

$$\tilde{P}_{\omega}(t) = (\chi^{(1)} + \frac{3}{4}\chi^{(3)}E^2)E\cos(\omega t) = (\chi^{(1)} + \frac{3}{4}\chi^{(3)}E^2)\tilde{E}(t)\,. \qquad (2.44)$$

The total refractive index can be expressed as

$$n = n_0 + n_2 I\,, \qquad (2.45)$$

where n_0 is the linear refractive index derived as

$$n_0 = \sqrt{1+\chi^{(1)}}\ , \qquad (2.46)$$

n_2 is the nonlinear refractive index, and I is the incident light intensity

$$I = \frac{1}{2}\varepsilon_0 n_0 E^2 c\,. \qquad (2.47)$$

According to Eq. (2.44), the total refractive index can be expressed as,

$$n = \sqrt{1 + \chi^{(1)} + \frac{3}{4}\chi^{(3)} E^2} \ . \tag{2.48}$$

With the substitution of Eqs.(2.46) and (2.47) into Eq. (2.48), Eq.(2.48) can thus be expressed as

$$n = \sqrt{n_0^2 + \frac{3}{2}\chi^{(3)} \frac{I}{\varepsilon_0 n_0 c}} = n_0 \sqrt{1 + \frac{3}{2}\chi^{(3)} \frac{I}{\varepsilon_0 n_0^3 c}} \approx n_0 (1 + \frac{3}{4}\chi^{(3)} \frac{I}{\varepsilon_0 n_0^3 c}) = n_0 + \frac{3\chi^{(3)}}{4\varepsilon_0 n_0^2 c} I \ . \tag{2.49}$$

By equating Eqs. (2.45) and (2.49), it can be found that

$$n_2 = \frac{3\chi^{(3)}}{4\varepsilon_0 n_0^2 2c} \tag{2.50}$$

where according to Eq. (2.40), $\chi^{(3)} = \chi^{(3)}(\omega; \omega, \omega, -\omega)$.

2.4.3 Self-Mode-Locking

If the nonlinear refractive index is positive, the total refractive index increases with the intensity. Since the center part of beam transverse profile has higher intensity than the edges, the refractive index at the center is larger than the edges. This leads to an increase of the beam confinement at the center, and the beam diameter becomes narrower. This effect is known as the Kerr lensing effect, which is illustrated in Fig. 2.7; a smaller beam diameter leads to decreased mode interaction with the external gold contacts, thus reducing the coupling waveguide losses. This results in a saturable loss mechanism, i.e., decrease in optical losses with increasing intensity, which is the fundamental ingredient for SML. In the presence of such a mechanism, it may become favorable for the laser to emit ultrashort pulses because of their higher instantaneous intensity and hence, lower losses relative to CW emission, in which the output energy is spread uniformly over time.

The pulse duration can be estimated using the theory of self-phase modulation (SPM) [43].

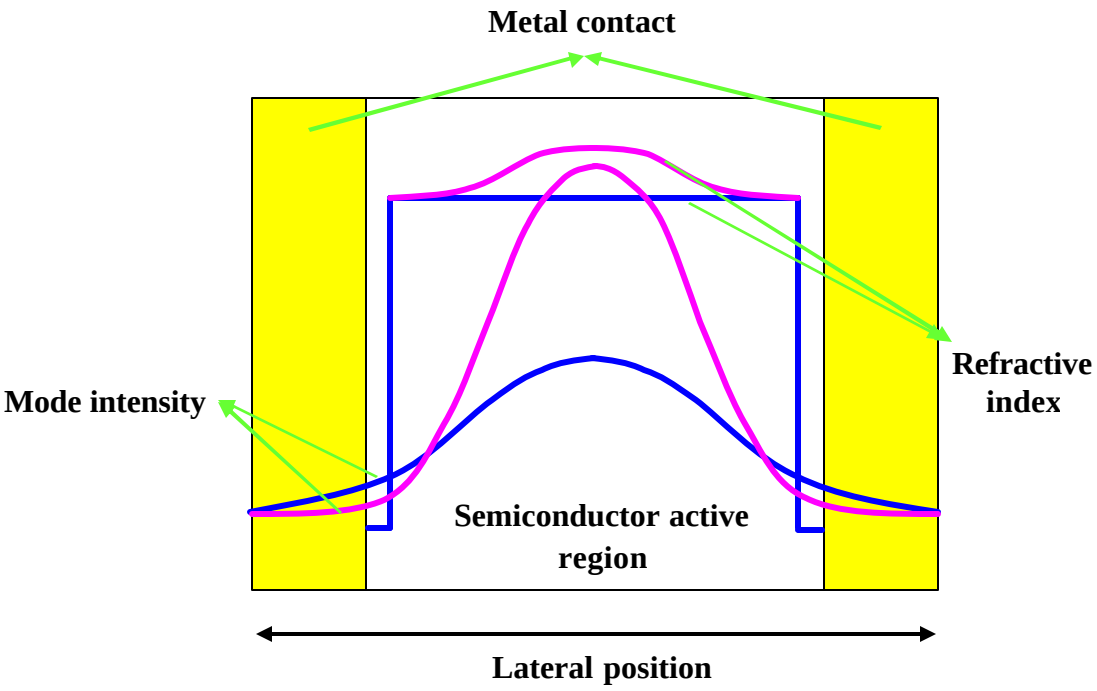

Figure 2.7 Illustration of Kerr-lensing effect.

Self-phase modulation describes the spectral response of a short optical pulse propagating through nonlinear optical medium. In order to understand the origin of this effect, let us start with the optical pulse with the form

$$\tilde{E}(z,t) = \tilde{A}(z,t)e^{i(k_0 z - \omega_0 t)} + c.c. \tag{2.51}$$

where *c.c.* denotes the complex conjugate propagating in the medium characterized by a nonlinear refractive index of the sort similar to Eq (2.45) but with instantaneous response to the pulse intensity,

$$n(t) = n_0 + n_2 I(t)\,, \tag{2.52}$$

where $I(t) = (n_0 c/2\pi)\left|\tilde{A}(z,t)\right|^2$. It is assumed that the nonlinear medium is sufficiently short that no reshaping of the optical pulse can occur within the medium; the only effect of the medium is to change the phase of the transmitted pulse by the amount

$$f_{NL}(t) = -2n_2 I(t) L \frac{w_0}{c}, \tag{2.53}$$

where L is the length of the nonlinear medium.

As a result of the time-varying phase of the wave, the spectrum of the transmitted pulse will be modified and typically will be broader than that of the incident pulse. The spectral content of the transmitted pulse can be calculated by the energy spectrum

$$S(w) = \left|\int_{-\infty}^{\infty} \tilde{A}(t) e^{-iw_0 t - i f_{NL}(t)} e^{iwt} dt\right|^2. \tag{2.54}$$

However, the spectral content can be more intuitively described by the concept of instantaneous frequency $w(t)$ of the pulse,

$$w(t) = w_0 + dw(t) \tag{2.55}$$

where

$$dw(t) = \frac{d}{dt} f_{NL}(t) \tag{2.56}$$

denotes the variation of the instantaneous frequency.

The use of the above analysis can be illustrated by an example. Suppose the pulse shape is given by the form

$$I(t) = I_0 \operatorname{sech}^2(t/t_0), \tag{2.57}$$

which is illustrated in Fig. 2.8(a), then from Eq. (2.53) the nonlinear phase shift is found as

$$f_{NL}(t) = -2n_2 \frac{w_0}{c} LI_0 \mathrm{sech}^2(t/t_0), \tag{2.58}$$

and from Eq. (2.56) the change in instantaneous frequency is given by

$$dw(t) = 4n_2 \frac{w_0}{ct_0} LI_0 \mathrm{sech}^2(t/t_0)\tanh(t/t_0). \tag{2.59}$$

The variation in the instantaneous frequency is illustrated in Fig. 2.8(b) with positive n_2. It is can be seen that the leading edge of the pulse is shifted to lower frequencies and that the trailing edge is shifted to higher frequencies. The frequency spectrum is shown in Fig. 2.8(c). The maximum value of the frequency shift is of the order of the order of

$$dw_{\max} \approx \frac{\Delta f_{NL}^{(\max)}}{t_0}, \tag{2.60}$$

where

$$\Delta f_{NL}^{(\max)} \approx 2n_2 \frac{w_0}{c} I_0 L. \tag{2.61}$$

A notable feature of SPM is that the induced spectral broadening is accompanied by an oscillatory structure covering the entire frequency range. To obtained a more accurate measure of spectral broadening, one should use the RMS spectral width Δw_{rms} defined as

$$\Delta w_{rms} = \sqrt{\left\langle (w - w_0)^2 \right\rangle - \left\langle (w - w_0) \right\rangle^2}, \tag{2.62}$$

The pulse duration can be estimated as [24],

$$t_p = \frac{\sqrt{2\log 2}}{\Delta w_{rms}} \sqrt{1 + \frac{4}{3\sqrt{3}} f_{\max}^2}. \tag{2.63}$$

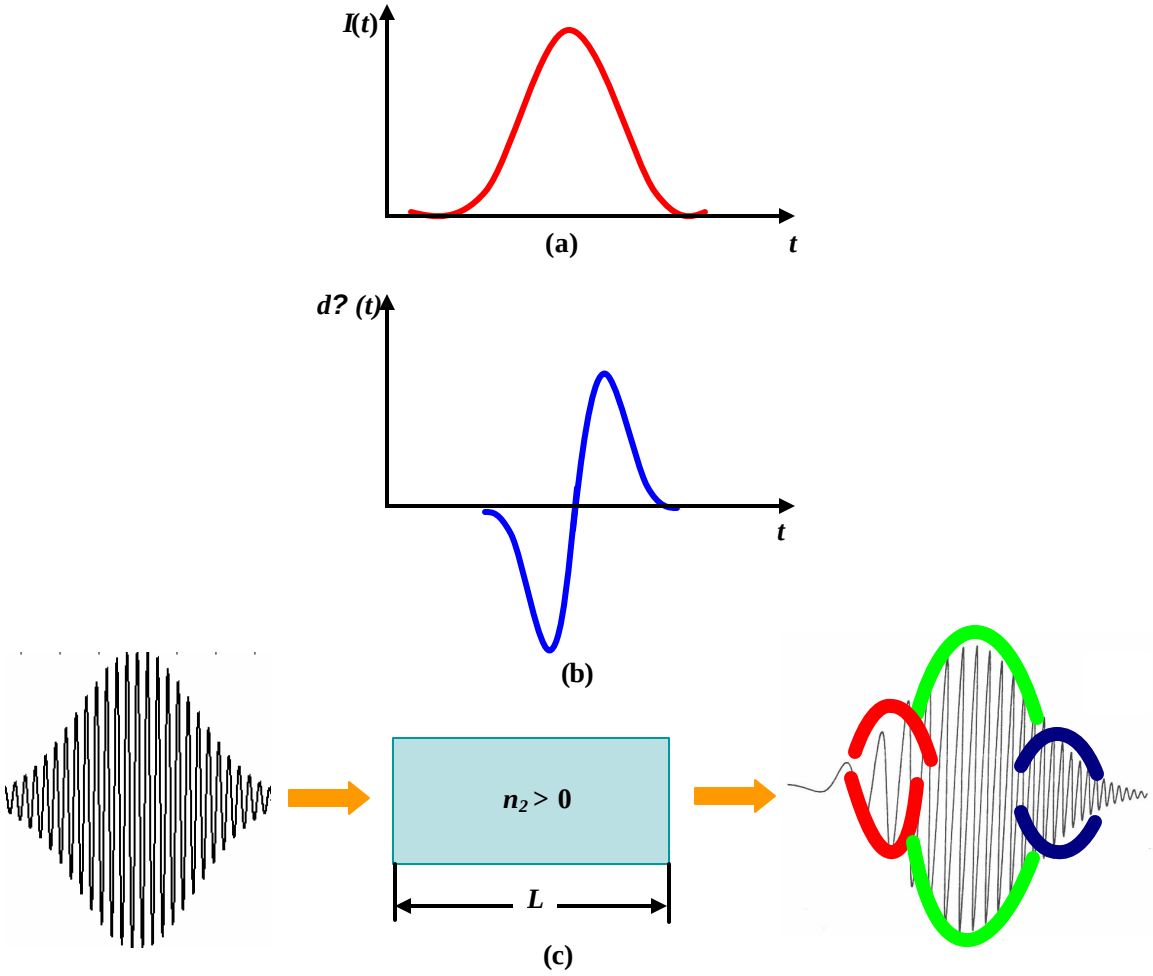

Figure 2.8 Illustration of self-phase modulation: (a) time dependence of incident pulse intensity; (b) change in instantaneous frequency of the trans mitted pulse; (c) spectral broadening due to self-phase modulation.

2.5 Rate-Equation Model and Density Matrix Approach

There has been much speculation about the nature of the electron transport in QCL's, i.e., coherence versus incoherent of the physical mechanism governing charge transport through injector/active-region/collector interfaces. The answer to this question touches upon the validity of our simulation approach to MIR QCL's.

The rate-equation approach is a semiclassical or Boltzmann-like treatment, in which the entire multiple QW is treated as a single quantum mechanical system with a

well defined Hamiltonian. All the subband energy levels are eigenstates (which are stationary by definition) of this Hamiltonian. The transport process is the collective effect of intersubband scattering between the various subbands (eigenstates) involved, and can be calculated using the Fermi's golden rule approximation. In this picture, there is no coherent oscillatory time evolution among the subband electron populations. The electron wavefunctions always correspond to the stationary eigenstates, and scattering transports an electron from one eigenstate to another. In this approach, the time evolution of electron population at each subband is governed by the Bolzmann-like equation,

$$\frac{dn_i}{dt} = \sum_{f \neq i} n_f W_{fi} - \sum_{f \neq i} n_i W_{if}, \tag{2.64}$$

where i, f run over all states and W_{fi} is the rate at which particles make the transition $f \rightarrow i$ which increase the population of level i, and, and similarly W_{if} is the rate at which particles make the transition $i \rightarrow f$ which depopulate the level i. The inelastic scattering mechanism in InGaAs/InAlAs system is via LO phonon scattering and e-e scattering which are described in Section 2.3. The scattering rate is also dependent on the subband populations through Fermi distributions. Due to the periodicity of the QC structure, the summation of Eq. (2.64) is just including the injector, active region and collector, which accounts for 1.5 periods of QCL. Periodic boundary conditions are applied assuming that the transition from the preceding collector to the active region is equivalent to that between the collector and the next active region.

In the rate-equation model, no quantum-mechanical effects, such as coherent resonant tunneling between adjacent states, have been considered. In order to include the coherent phenomenon into the scenario, density matrix formalism is proposed as an

extended semiclassical simulation scheme [44]. In this approach, the basic ingredient is the single-particle density matrix ρ_{ij}. The time evolution of density matrix element is given by

$$\frac{d\rho_{ij}}{dt} = -i\omega_{ij}\rho_{ij} + \sum_{i'j'}\left[\left(\Gamma^{in}_{ij,i'j'}\rho_{i'j'} - \Gamma^{out}_{ij,i'j'}\rho_{i'j'}\right) + c.c.\right]. \tag{2.65}$$

where $\hbar\omega_{ij} = E_i - E_j$ is the energy difference between states i and j. The first term describes the coherent evolution of the noninteracting carrier system while the second contribution describes energy relaxation as well as dephasing due to the elastic intrasubband scatterings, in terms of generalized in- and out-scattering superoperators G [44]. The diagonal parts of matrices in Eq. (2.65) link to the semiclassical terms in Eq. (2.64): the diagonal parts of G matrices, i.e., $ii' = jj'$ correspond to the semiclassical scattering rates in Eq. (2.64), $\Gamma_{ii,i'i'} \equiv W_{ii'}$; similarly, the diagonal parts of population density matrix ρ_{ii} correspond to the electron population n_i at subband i in Eq. (2.64). The off-diagonal terms ($i \neq j$) describe the degree of quantum-mechanical phase coherence between states i and j. So Eq. (2.65) is the desired quantum-mechanical generalization of the Boltzmann transport equation in Eq. (2.64). Analogous to the rate-equation approach, the density matrix formulism also adopts the same periodic conditions to close the circuit.

In the current MIR QCL structure, the quantum-mechanical coherence effects can be ignored and the rate-equation model is employed for the simulation since it is well established that the rate equation is a reasonable approximation to the density matrix approach in view of the following points.

Due to the rapid scattering and photon lifetime, it is adequate for the most part to evaluate the output optoelectronic properties based on the steady-state solution to the

Boltzmann equation. Thus, it is important to check the relationship between the steady-state solutions from the two approaches. In the density matrix formulism presented in Chapter 3 of Ref. [42], the optical properties, such as the absorption (gain) coefficient, nonlinear susceptibilities $c^{(2)}$ and $c^{(3)}$, *etc.*, are calculated based on the zeroth order steady-state solution of density matrix element r_{mn}^{0}, exampled as Eq. (3.6.17) on Page 166 of Ref. [41]. Referring to pages 153 and 149 of [42], r_{mn}^{0} is just the equilibrium population of the system, and the off diagonal density matrix elements at equilibrium $r_{mn}^{0}(m \neq n)$ is vanish, i.e., there is no coherence produced in thermal equilibrium. Thus, the steady-state population obtained from rate-equation is the same as the zeroth order steady-state population that solved from the density matrix element. It can therefore be concluded that calculation of those optical properties by substituting the steady-state electron populations solved from the rate-equation model is valid.

Another check is carried out based on the comparison between the Rabi oscillation frequency and the FWHM transition linewidth. If the intersubband Rabi frequency n between resonant tunneling states i and j is much less than the transition lindwidth g_{ij} between them, it means that the Rabi oscillation between the two subbands will be quickly damped by the intersubband transition. In this case, the coherence between tunneling states is weak and thus the off-diagonal matrix elements in density matrix can be ignored. In the QCL structure under study, the Rabi frequency between the lasing states is estimated to be 0.76 THz, and the FWHM line broadening is 15.17 THz. This gives $n/g_{ij} \leq 0.05$ for the respective off-diagonal density matrix element. Thus, the

off-diagonal matrix elements can be safely ignored. This concludes that the rate-equation model is likely to provide a good approximation to the full density matrix.

There are several published works that comment on the coherence effect in MIR QCL's and validity of semiclassical rate-equation model. In [44], it was found that for typical QCL structures, energy-relaxation and dephasing processes are sufficiently strong to destroy any phase-coherence effect on a sub-picosecond time scale; as a result, the usual semiclassical or incoherent description of stationary charge transport is found to be in excellent agreement with experiments. As a practical matter, in [18] and [19], rate-equation models have been demonstrated to be quite successful in modeling MIR QCL's and simulation results agree well with the experiment findings.

CHAPTER 3

SUPERSYMMETRIC OPTIMIZATION OF QUANTUM CASCADE LASERS

This chapter presents the design procedure for MIR QCL's with optimized SHG. The optimization is carried out based on the structure repored in [16], which is designated the *original structure* in the following. It is a multiresonant subband electronic structure designed in order to enhance the SHG. The physical structure is composed of InGaAs QW's and AlInAs barriers, both lattice mattached to an InP substrate. The fundamental emission wavelength is at 9.1 μm and SHG is at 4.55 μm. The optimized design is obtained utilizing techniques from SUSYQM with both material-dependent effective mass and band nonparabolicity. Carrier transport and power output of the structure are analyzed by self-consistently solving rate equations for the carriers and photons. Nonunity pumping in the carrier transport and the phase mismatch in the wave propagation are included in the model.

3.1 Band Structure Analysis

The bandstructure analysis is the starting point for analyzing any quantum devices. In the current model, the band structure is solved using the finite-difference method, in which spatially dependent mass and band nonparabolicity are included. The Schrödinger equation is

$$-\frac{\hbar^2}{2}\frac{d}{dx}\left(\frac{1}{m^*(x,E)}\frac{dy(x)}{dx}\right)+V_0(x)y(x)=Ey(x). \qquad (3.1)$$

where $\hat{x}$ is QW layers growth direction and $V_0(x)$ is the energy profile for the original structure. With the expression of effective mass as Eq. (2.9), the above equation is formed as

$$\left[-\frac{\hbar^2}{2}\frac{d}{dx}\left(\frac{1}{m^*(x)}\frac{d}{dx}\right)+V_0(x)\right]y(x)=\left[\frac{2gm^*(x)}{\hbar^2}E(E-E_{cbm})+\left(1-\frac{2gm^*(x)}{\hbar^2}V_0(x)\right)(E-E_{cbm})\right]y(x), \tag{3.2}$$

where g is the nonparabolicity coefficient, $m^*(x)$ is the effective mass of the QW at the bottom of the conduction band, and E_{cbm} is the energy at the conduction-band bottom.

Equation (3.2) is a quadratic eigenvalue problem (QEP). In order to avoid the mathematical complexity for solving QEP, the band structure is solved through a trial energy process as shown in Fig. 3.1.

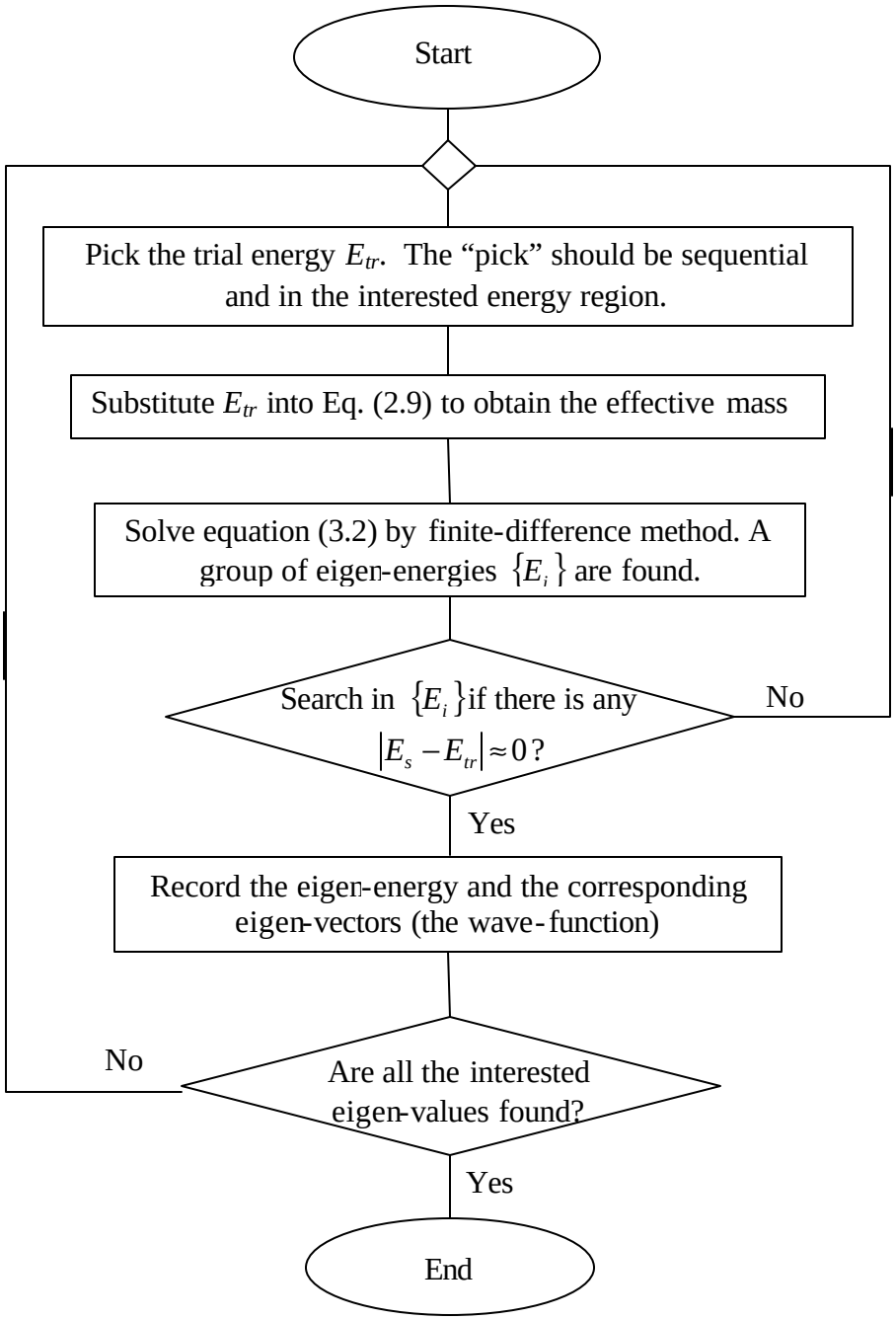

Fig. 3.1 Solution procedure for the band structure with nonparabolicity.

The finite-difference method is one of the most important and simplest ways of approximating differential operator and transforming differential equations into linear eigen-value problem. In finite different method,

$$\frac{dy(x)}{dx} \approx \frac{y(x+h)-y(x)}{h} \qquad (h \to 0) \tag{3.3}$$

and

$$\frac{d^2y(x)}{dx^2} \approx \frac{d}{dx}\left(\frac{dy(x)}{dx} - \frac{dy(x-h)}{dx}\right) = \frac{y(x+h)-2y(x)+y(x-h)}{h^2} \quad . \tag{3.4}$$

When Eq. (3.4) is inserted into Eq. (3.1) by representing continuous function $y(x)$ by a series of discrete values $y(x_i)$, where i =1, 2, 3, ..., N for segments on x line, Eq. (3.1) becomes linear function with the matrix form of

$$A_{ji}\{y_i\} = E\{y_i\}, \tag{3.5}$$

which can be solved by the linear eigenvalue problem, with eigenvalue E as the subband energy level and eigenfunction $\{y_i\}$ as corresponding wavefunctions. The obtained wavefunctions and subband energy levels for the original structure are denoted as $y^0_{(k)}$ and $E^0_{(k)}$ respectively, where k represents different subbands.

The band structure calculated for the original structure is shown in Fig. 3.2, which agrees well with the results shown in [16]. The band structure calculated contains all active portions of which are accounted for in the rate-equation model described in next section, i.e., an active region, an injector, and a collector, which is equal to 1.5 periods of the full cascade. There are totally 15 $(1 \le k \le 15)$ energy levels retained. The injector and collector regions are represented by five energy levels each, i.e. subbands 1, 2, 4, 5, and 7 for collector and subbands 8, 10, 11, 12, and 13 for the injector. The active region, where

laser emission and SHG take place, has 5 energy levels, i.e., subbands 3, 6, 9, 14, and 15. Radiative transitions occur between the third and second states in the active region, denoted as 9 and 6, while level 3 is the ground state in the active region. Levels 6, 9, 14, and 15 constitute two nonlinear cascades: 6-9-14 for cascade I and 9-14-15 for cascade II.

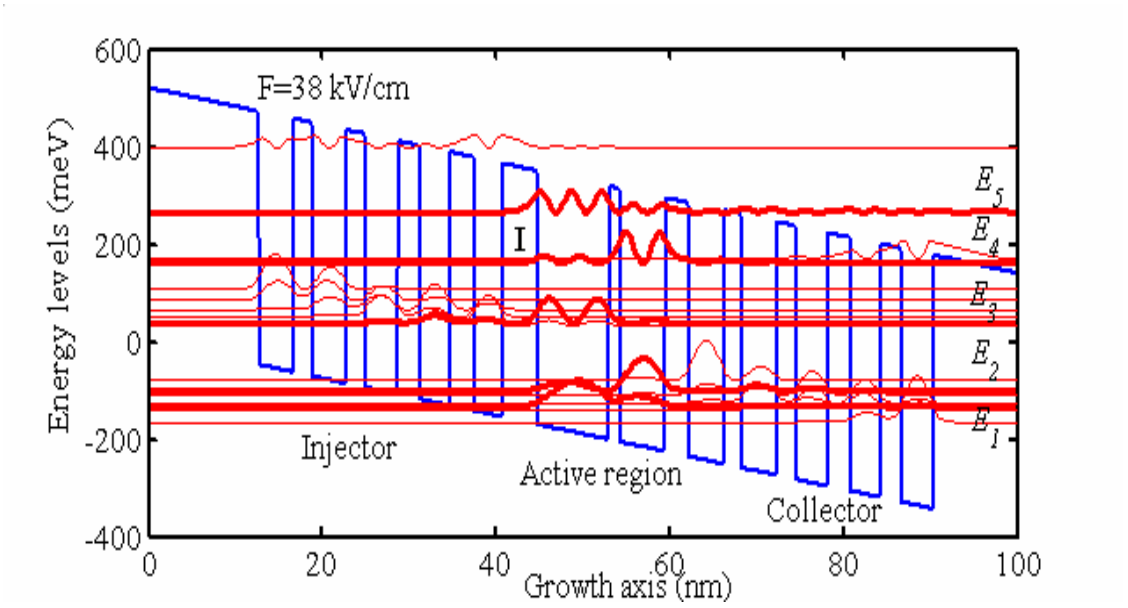

Figure 3.2 Computed band structure for the original structure.

3.2 Supersymmetric Optimization for Second-Harmonic Generation

The optimized is targeted to improve the figure of merit of SHG, i.e., the second-order nonlinear susceptibility $c^{(2)}$ with expression as

$$c^{(2)}(2w) \approx \frac{2pe^3}{e_0}\left[\frac{M_{23}M_{34}M_{24}}{E_{42}-2\hbar w-ig_{42}}\left(\frac{n_3-n_4}{E_{43}-\hbar w-ig_{43}}+\frac{n_3-n_2}{E_{32}-\hbar w-ig_{32}}\right)\right.$$
$$\left.+\frac{M_{34}M_{45}M_{35}}{E_{53}-2\hbar w-ig_{53}}\left(\frac{n_4-n_5}{E_{54}-\hbar w-ig_{54}}+\frac{n_4-n_3}{E_{43}-\hbar w-ig_{43}}\right)\right], \quad (3.6)$$

where M_{ij} is the dipole matrix element between levels i and j, n_i is electron population density at level i, and $E_{ij}=E_i-E_j$ is the energy separation between levels i and j and $2g_{ij}$ is the FWHM of the transition broadening between levels i and j.

From Eq. (3.6), it can be seen that $c^{(2)}$ is proportional to the dipole matrix element products $M_{23}M_{34}M_{24}$ for cascade I and $M_{34}M_{45}M_{35}$ for cascade II, and inverse proportional to the energy detuning between resonant levels. The optimization strategy is to maximize the dipole matrix element products while keeping ther resonant energy levels unchanged.

The nonlinearity can be optimized by systematically changing the band structure through the QW potential. The method used here is SUSYQM [45]. It enables one to generate a family of potentials depending on a single parameter l isospectral to the original one thus preserving the multiple resonances enabling SHG as well as energy-level positions that facilitate relaxation and tunneling from period to period of the QCL structure.

The supersymmetric partner of $V_o(x)$ is given by [45],

$$V_s(x) = V_o(x) - \frac{\hbar^2}{\sqrt{m^*(x)}}\frac{d}{dx}\left[\frac{1}{\sqrt{m^*(x)}}\frac{d}{dx}\{\ln[l + I(x)]\}\right], \tag{3.7}$$

with $I(x) = \int_{-\infty}^{x} q^2(t)dt$ and $q(x) = y_{(k)}^{0}(x)$. From Eq. (3.7), it can been seen that the isospectral potential is obtained through the base function $q(x)$, which is chosen from one of the wavefunctions $y_{(k)}^{0}(x)$. The modified wavefunctions can be expressed as

$$y_{(k)}^{ss}(x; l) = y_{(k)}^{0}(x)\sqrt{l(l+1)}\Big/[l + I(x)], \tag{3.8a}$$

$$y_{(i)}^{ss}(x; l) = -y_{(i)}^{0}(x) + y_{(i)}^{0}(x)[l + I(x)]^{-1}\int_{-\infty}^{x} dt\, y_{(k)}^{0}(t)y_{(i)}^{0}(t) \text{ with } i \neq k. \tag{3.8b}$$

The modified dipole matrix element products relating to $c^{(2)}$ is then calculated based on modified wavefunctions in (3.8a) and (3.8b) with variation of parameter l. The

relationship between dipole matrix elements products and l is then plotted with different base functions. Best base function $q(x)$ is selected by comparing optimization effects.

SUSYQM has been used for the optimization of the intersubband resonant $c^{(2)}$ for the harmonic oscillator in [27]. In that work, the initial SUSYQM calculation does not include band nonparabolicity. With band nonparabolicity included, the SUSYQM optimized potential has to be slightly tailored in order to restore the levels' equidistance. The improvement of dipole matrix element product is about 20 % in that work. In the current work, to include the band nonparabolicity, the effective mass $m^*(x)$ in Eq. (3.7) is replaced by the energy-dependent effective mass $m^*_{np}(x, E_k)$ with a form similar to Eq. (2.9),

$$m^*_{np}(x, E_k) = m^*(x)(1+\frac{2gm^*(x)\times(E_k - E_{cbm})}{\hbar^2}), \tag{3.9}$$

The l-value range is $l \le -1$ and $l \ge 0$ l to maintain continuity of wavefunctions [46]. By inspection, there are two groups of $q(x)$ with the optimized l-value l_{opt} giving best optimization, as shown in Fig. 3.3: (i) for $q(z) = y^{0}_{(6)}(z)$ and $l_{opt} = 0.6$, there is a maximum dipole matrix element product $M_{69}M_{9(14)}M_{6(14)}$ for cascade I, which is estimated to be about 20 % higher than that with the original potential shape, while that for cascade II remains constant; (ii) for $q(x) = y^{0}_{(15)}(x)$ and $l_{opt} = 0.6$, the maximum $M_{9(14)}M_{(14)(15)}M_{9(15)}$ for cascade II exceeds by 20 % the original value, while that for I remains constant. In Fig. 3.3, M_{opt} and M_{org} represent the optimized and original dipole matrix element products respectively, with $M_{69}M_{9(14)}M_{6(14)}$ for cascade I and

$M_{9(14)}M_{(14)(15)}M_{9(15)}$ for cascade II. According to Eq. (3.1), the largest electron population lies in level 3, so the role of cascade I is much greater than that of cascade II, and group (i) is selected to determinate the optimized potential.

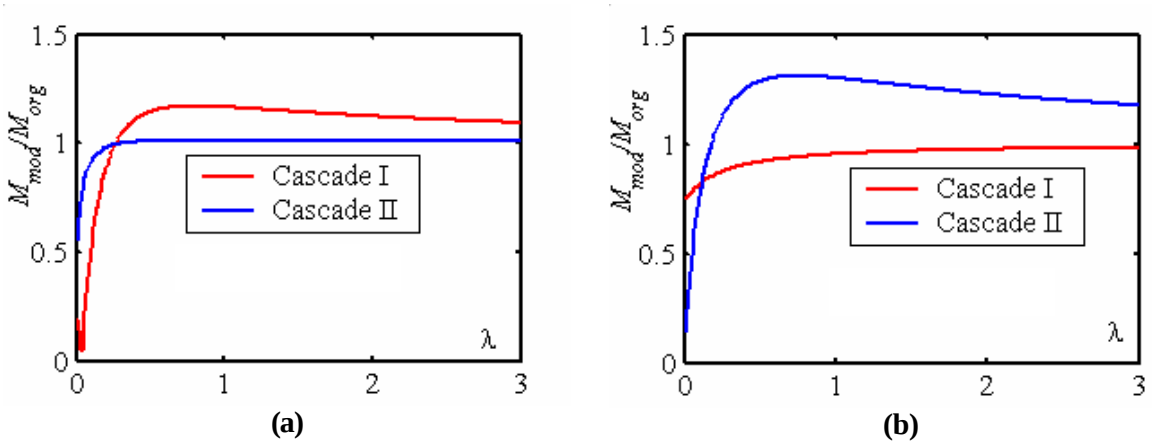

Figure 3. 3 Dependence of dipole matrix element product on l :
(a) $q(x) = y_0^{(6)}(x)$ **; (b)** $q(x) = y_0^{(15)}(x)$

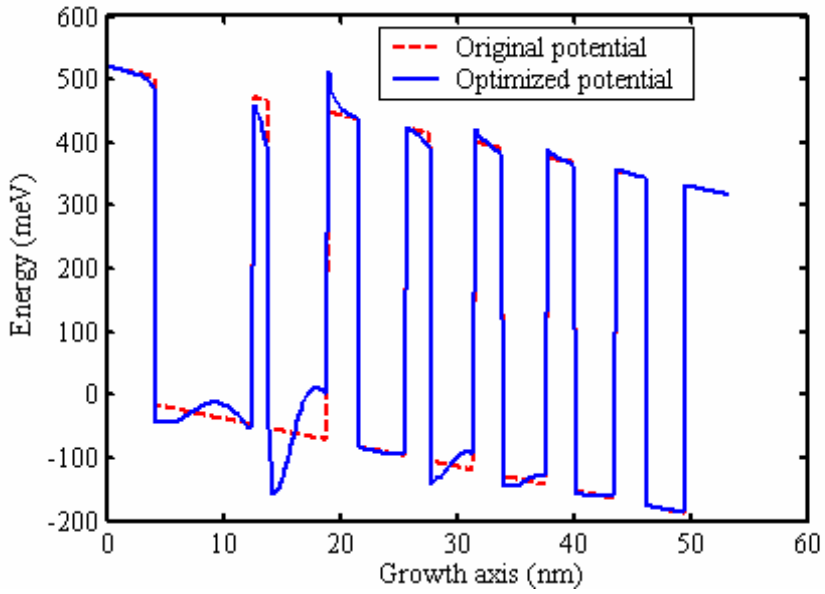

Figure 3.4 Optimized potential and original potential.

The optimized potential from SUSYQM is shown in Fig. 3.4. It can be realized by modifying the mole fraction of constituents of the ternary alloy, i.e.,

$E_g = 324 + 700x + 400x^2 (meV)$ for $Ga_xIn_{1-x}As$ and $E_g = 357 + 2290x$ (meV) for $Al_xIn_{1-x}As$ [47]. According to SUSYQM, the optimized structure is isospectral to the original structure for all energy levels. This is the case for the optimized structure with ideally smooth curvature resulting from continuously compositional grading. Due to low growth efficiency, in practice, instead of employing continuous graded-index materials, the structure can be fabricated by digital-alloy growth technique [48], which overcomes the technical difficulties of continuous grading the alloy composition. In digital alloy technique, the digitization period (DP) is the thickness of each growth layer with the same composition, i.e., the step size in digital growth. The smaller the DP, the better the approximation. With the development of digitally grown submonolayer superlattices (SMS) by excellent growth condition control [49], DP can be down to around one half of the monolayer thickness *a* for InGaAs/AlGaInAs superlattices structure. The monolayer thickness can be the upper borderline of the potential curvature roughness for the SMS. In order to study the influence of digital growth step size on the ideally optimized structure, apart from the model with ideally curved profile, models are also built for with half-monolayer DP and monolayer DP. For the model with half-monolayer DP, the stepwise grading not only changes the dipole matrix element products , but also displaces the subbands so their spacings deviate from the desired values, with E_{96} = 125meV instead of 131 meV, $E_{(14)9}$ = 131 meV instead of 123 meV, and $E_{(15)(14)}$ = 90 meV instead of 105 meV. The energy gap $E_{(15)9}$, however, is still in strong resonance with that E_{96}, even though $E_{(15)(14)}$ deviates a little more. Thus, there is still considerable SHG produced by this structure. The fundamental emission wavelength has a slight red shift of 0.46 μm, while that for SHG is 0.92 μm. In the monolayer DP model, all the original resonant

states are destroyed with E_{96} = 120 meV, $E_{(14)9}$ = 52 meV and $E_{(15)(14)}$ = 152 meV. It is found that profile roughness has more influence on the energy states rather than on the dipole matrix element. Figure 3.5 (a) shows the band structure of the original structure and optimized structure with half monolayer DP, while fig 3.5(b) shows the digitization of the optimized profile in comparison with the original and ideally optimized profiles.

The material system $Ga_{0.47}In_{0.53}As/Al_{0.48}In_{0.52}As$ is lattice-matched to the InP substrate. For ternary alloys GaInAs/AlInAs, the mole fraction not only changes the bandgap, but it also alters the lattice constant *a*. Thus, there will be strain generated in the structure with the modified potential. For ternary alloy $A_xB_{1-x}C$, *a* is calculated by $a = a_{AC}\,x(z) + a_{BC}(1 - x(z))$. The lattice-constant mismatch affects the band structure of the QW, which was included in the $k \cdot p$ method [50]. The strain is evaluated based on the relative lattice constant difference between adjacent elements layers in the finite different method [48]. The strain tensor can be derived as $e_{xx} = e_{yy} = e_i$, and $e_{xx} = -2e_i\, C_{12}/C_{11}$. The conduction-band energy shift is determined by the strain tensor by $DC = C_1(e_{xx} + e_{yy} + e_{zz})$, in which C_1 is the deformation potential for the conduction band. With the optimized potential $V_{opt}(x)$, the total Hamiltonian for the conduction band for the strained lattice can be written as [50],

$$H_{tot} = -\frac{\hbar^2}{2}\frac{d}{dx}\left(\frac{1}{m^*(x,E)}\frac{d}{dx}\right) + V_{opt}(x) + \Delta C\,. \tag{3.10}$$

In the current model, the maximum strain between adjacent layers is ~ 1 %, while the total strain for the whole one module of the QCL structure is < 0.01 %. The optimized structure is strain compensated.

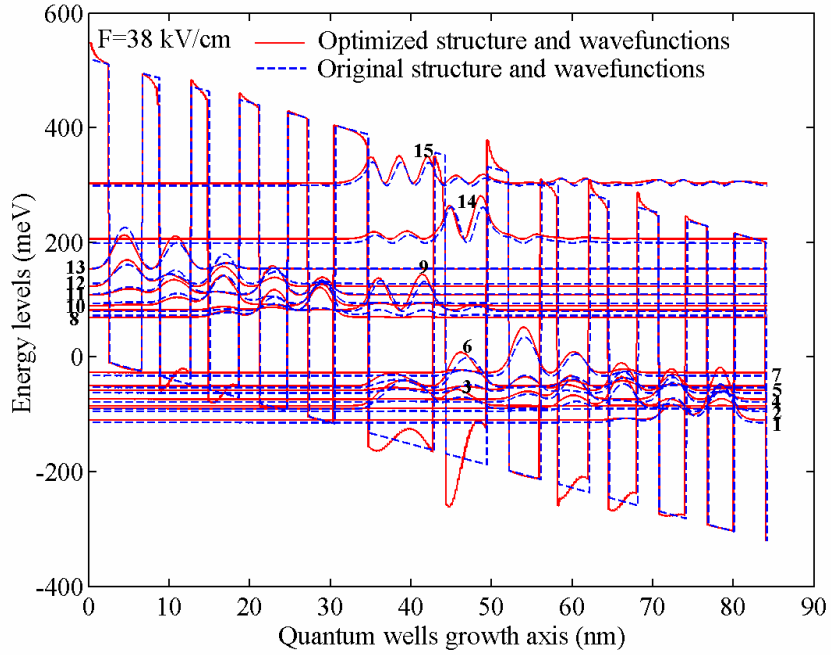

(a)

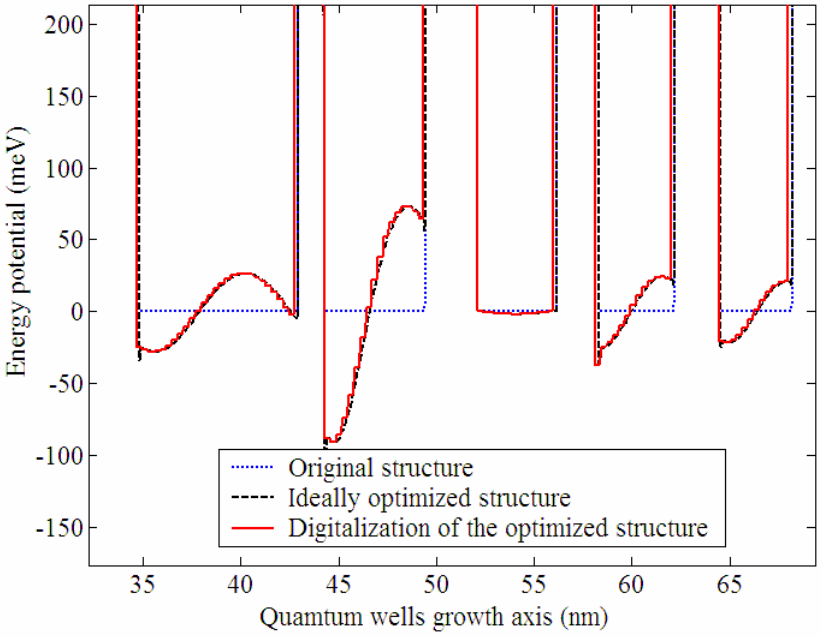

(b)

Figure 3.5 (a) Original and optimized band structures with corresponding potential shapes; (b) digitally graded energy potential in comparison with the original and ideally optimized potentials.

Here we briefly discuss the concern on interface roughness scattering brought by the thin layers grown by the digital growth technique. As discussed in [26] with the experimental evidence of [51], since the layers in digital alloy are not confinement layers, but rather act via the average composition, with wave functions evenly penetrating the well and barrier slices, the width fluctuations should average out, with no significant effect on the wave function shapes. So one may expect limited broadening of intersubband transitions.

The calculations show that the dipole matrix element product for cascade I is enhanced by 60 % over the original value, while that for cascade II remains unchanged. As shown in Fig. 3.5(a), the eigenfunction for the second subband changes the most. The dipole matrix element M_{32} increases by 35 % compared with the original value. This leads to larger oscillator strength between the lasing levels.

It is also important to verify if the enhancement is robust against changes in the electric field within the cascade. We therefore checked the dipole matrix element products' variation with electric-field. For the optimized structure with half monolayer DP, the dipole matrix element product ratio M_{opt}/M_{org} for cascade I oscillates around 1.6 with a value > 1.3 within the electric-field range 10-48 kV/cm, and the ratio for cascade II is between 0.8 and 1.10. The maximum change of energy spacings is within the FWHM of the device. Since the electric field changes only slightly above threshold, the dipole matrix elements enhancement as well (as the energy levels) does not change much within the operation range of electric field.

Due to the population redistribution amongst the levels, there will be competition between gain and $c^{(2)}$, but the increased oscillator strength between lasing levels may alleviate the competition. In order to further investigate the influence on the modal gain by the SUSYQM modified potential, a dynamic analysis for the lasing performance is performed through self-consistent rate equations.

3.3 Rate-Equation Model

A rate-equation model for a typical QCL structure without SHG was studied in Ref. [18]. The current 15-level dynamic model for the QCL structure not only incorporates SHG within the full cascade scheme, but also the interplay between time-varying photon density and radiative transition rates. Investigation also goes for the device performance for applied bias field between 30 kV/cm and 50 kV/cm, which is around the cascading bias 38 kV/cm. Since energy-level ordering among the three regions varies with the applied bias, the band structure at 38 kV/cm bias is taken to illustrate the rate-equation approach. Results from the rate-equation model for the original structure matches well the experimental results in [16].

3.3.1 Intersubband Transition Mechanisms

In the active region, the states 6, 9, 14, and 15 are equally spaced, and the energy intervals are resonant with the lasing frequency. In addition to the single photon absorption and emission, the involvement of SHG resonant levels, i.e., 6-9-14 and 9-14-15 brought both sequentially and simultaneously resonant intracavity two-photon processes. In the self-consistent rate-equation model, the quantum mechanical description of two-photon processes given in Ref. [42] is adopted. Two-photon absorption between states $9 \rightarrow 15$ and emission between $14 \rightarrow 6$ tend to degrade the lasing performance due

to the reduced population inversion between lasing states 6-9. The single-photon and two-photon processes are all incorporated into the rate-equation model in order to investigate the lasing output. Three-photon processes should also exist for the triply harmonic resonant levels 6-9-14-15, but the scattering rate is estimated to be on the order of $10^8 s^{-1}$, which is negligible compared to single-photon and two-photon transition rates on the order of $10^{11} s^{-1}$

The single-photon stimulated emission rate is expressed as,

$$W_{nm}^{p} = \frac{e^2 M_{nm}^2 w}{e} \frac{g_{nm}}{(E_{nm} - \hbar w)^2 + g_{nm}^2} m_w , \tag{3.11}$$

where m_w is the photon density (m^{-3}), M_{nm} is the dipole matrix element between levels *n* and *m*, $2g_{nm}$ is the FWHM of the $n \to m$ transition with the value taken from experimental measurements in Ref. [16], E_{nm} is energy difference between levels *n* and *m*, e is the permittivity of the lasing medium and w is incident photon frequency. Unlike the single-photon transition rate, which is proportional to the incident photon density (light intensity), the two-photon stimulated emission/absorption rate is proportional to the squared photon density. With the two-photon transition cascade *g-m-n*, the two-photon stimulated emission/absorption rate is given by [42],

$$W_{ng}^{2p}(w) = \frac{e^4 M_{nm}^{\ 2} M_{mg}^{\ 2}}{2\hbar e^2} \left(\frac{\hbar w}{E_{mg} - \hbar w} \right)^2 \frac{g_{ng}}{(E_{ng} - 2\hbar w)^2 + g_{ng}^2} m_w^{\ 2} , \tag{3.12}$$

The QCL is formed by several repetitions of the given unit cell. If neglect effects associated with the initial and final few periods are neglected, the carrier populations in the various levels will be periodic in the growth direction throughout the QCL. To introduce periodic boundary conditions, the technique presented in [18] is employed.

Namely, with the translational repetition of 1.5 cascade periods, carriers populate the injector subbands by transferring from the preceding active region and leaving the collector subbands to enter the subsequent active region. The transition between the preceding injector region and active region is equivalent to that between the collector region and the next active region. In order to use the injector-active region-collector to reflect the full periodic cascade structure, the population in subband 1 must be equivalent to the population in subband 8, as well as $2 \rightarrow 10$, $4 \rightarrow 11$, $5 \rightarrow 12$, and $7 \rightarrow 13$. Thus, the rate equations for the subbands in the injector region are equivalent to those for the collector region, and the steady-state subband populations for the injector are equal to those of the collector.

Except for the radiative single-photon and two-photon processes for resonant levels in the active region, LO phonon scattering and e-e scattering are the main scattering mechanisms for transitions within each region and transport between the injector-active region or active region-collector. When the energy separation between the levels is much smaller than the LO phonon energy, elastic electron-electron scattering dominates. For the resonant tunneling transitions between the injector and upper lasing level or between the lower lasing level and the collector, e-e scattering plays an important role. For the scattering rate calculation, the formulation described in Section 2.3 is adopted, in which LO phonon scattering rate is calculated using Fermi's golden rule with the Fröhlich interaction Hamiltonian, and the e-e scattering rate is calculated with form factors given by the overlap of the wavefunctions from the initial and final states. For both scattering mechanisms, both momentum and energy are conserved during carrier transitions. The transition rate between two states is both momentum dependent and

energy dependent. The total transition rate between two subbands is obtained by integration of the transition rates over all possible initial and final states. The electron distribution at each subband is taken to be quasi-Fermi distribution that depends on the subband Fermi energy [38], which in turn depends on the subband carrier density. The interplay between the scattering rates and electron population at each subband is connected through the Fermi energy at each subband until arriving at the steady-state. The state blocking effect is considered by the Pauli exclusion factor in term of Fermi's distribution function. Due to the small overlap between wavefunctions in the injector and collector subbands, the transition rates between injector and collector regions are neglected.

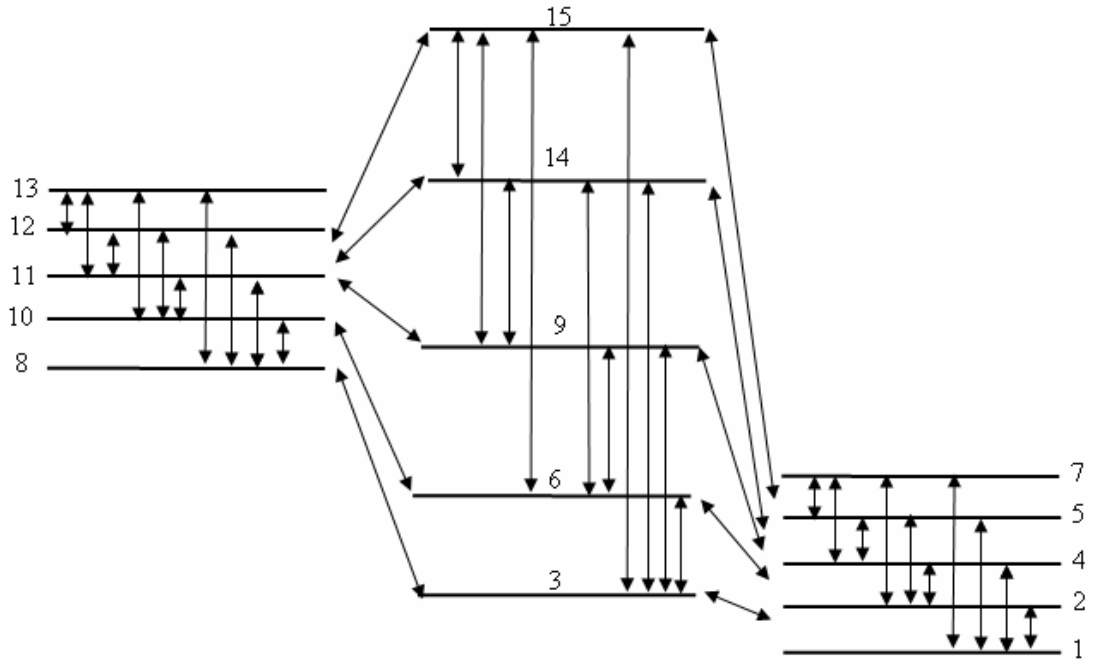

Figure 3.6 Illustration of carrier transitions in the 15-level system.

As shown in Fig. 3.6, two-way transitions are included between any of the two subbands, so the thermal backfilling is accounted in the theoretical model. For the transition between any two levels of the nonlinear cascade 6-9-14-15 in the active region,

the total scattering rate includes not only the nonradiavie ones, but also the radiative single-/two-photon transitions, which are linearly and/or quadratically dependent on the incident photon density. For transition rates between the adjacent single-photon resonant levels, i.e., W_{69}, W_{96}, $W_{9(14)}$, $W_{9(14)}$, $W_{(14)(15)}$ and $W_{(15)(14)}$, one has

$$W_{ij} = W_{ij}^{LO} + W_{ij}^{e-e} + W_{ij}^{p}, \tag{3.13}$$

where W_{ij}^{p} can be obtained from Eq. (3.11), and it makes W_{ij} depend linearly on the photon density in the lasing cavity. Similarly, for transition rates between two-photon resonant levels, i.e., $W_{6(14)}$, $W_{(14)6}$, $W_{9(15)}$, and $W_{(15)9}$, one obtains

$$W_{ij} = W_{ij}^{LO} + W_{ij}^{e-e} + W_{ij}^{2P}, \tag{3.14}$$

where W_{ij}^{2p} can be obtained from Eq. (3.12), and this makes W_{ij} has quadratic dependence on the incident photon density. For the transition between any other subbands, the transition rate is the sum of the e-e and LO phonon scattering rates and thus independent of the photon density in the cavity.

3.3.2 Rate-Equation Formulation

The rate-equation is built based the population variation at each subband due to various electron scattering mechanisms. As an example for the subband populations in the injector/collector region, the rate equation for subband 1 is written as

$$\frac{dn_1}{dt} = \sum_j (W_{j1} n_j + W_{j8} n_j - W_{1j} n_1 - W_{8j} n_8) + \sum_k (W_{k1} n_k - W_{1k} n_1), \tag{3.15}$$

where W_{pq} represents the total scattering rate between subbands p, and q. In the above expression, indices $j = 3, 6, 9, 14, 15$ and $k = 2, 4, 5, 7$. The rate equation is similar for

any other injector or collector state. The rate equation for the subband population in the active region is given by

$$\frac{dn_j}{dt} = \sum_{i=1, i\neq j}^{15} \left(W_{ij} n_i - W_{ji} n_j\right), \tag{3.16}$$

where $j = 3, 6, 9, 14, 15$.

The rate equation for density of photons resulted from both the single- and two-photon processes are as follows,

$$\frac{dm_w}{dt} = \Gamma\left[W_{96}^{p}(n_9 - n_6) + W_{(15)(14)}^{p}(n_{(15)} - n_{(14)}) + W_{(14)9}^{p}(n_{(14)} - n_9)\right],$$

$$+ 2\Gamma\left[W_{(15)9}^{2p}(n_{15} - n_9) + W_{(14)6}^{2p}(n_{14} - n_6)\right] - \frac{m_w}{t_p^w}, \tag{3.17}$$

where Γ is the mode confinement factor, which is assumed to be 0.5, and t_p^w is the photon lifetime related to the total loss as $t_p = (v_g a_w)^{-1}$ [52].

The set of 16 rate equations involves electron populations on 15 subbands together with the photon density. As shown in Eq. (3.17), the photon density variation depends on the transient scattering rates and subband electron populations in the active region, while the radiative scattering rates are also linearly or quadratically dependent on the photon density in the cavity as shown Eq. (3.11) and (3.12). Apart from this, in each subband, there is also the interplay between the electron population and scattering rates, which are connected by the quasi-Fermi distribution functions. The steady-state electron populations and photon density are achieved by iteratively solving the whole set of 16 rate equations.

The current density through injector-active region interface is given by

$$J_{IA} = J_{I3} + J_{I6} + J_{I9} + J_{I(14)} + J_{I(15)}. \tag{3.18}$$

The component current density J_{Ii} (i = 3, 6, 9, 14, 15) is the difference between the scattering current density from the injector region to the level i of the active region and the backscattering from this level i to the injector region, i.e.

$$J_{Ii} = J_{I\to i} - J_{i\to I} = q\sum_k (W_{ki} n_k - W_{ik} n_i), \tag{3.19}$$

where k = 8, 10, 11, 12, 13 represents levels in the injector region. Similarly, current density flow from the active region to the collector region can be written as

$$J_{AC} = J_{3C} + J_{6C} + J_{9C} + J_{(14)C} + J_{(15)C}, \tag{3.20}$$

where the component J_{iC} is the difference between the scattering current from the level i in active region to the collector and backscattering from collector to the level i, i.e.

$$J_{iC} = J_{i\to C} - J_{C\to i} = q\sum_k (W_{ik} n_i - n_k W_{ki}). \tag{3.21}$$

The current densities described above are evaluated based upon the steady-state electron populations and scattering rates. At steady-state, this is $J_{iA} = J_{AC} = J$.

3.3.3 Linear and Second-Harmonic Wave Propagations and Power Outputs

Once the subband populations in the lasing levels at steady state are found, the net modal gain can be calculated as

$$G_m^{net} = \frac{G\, 4\pi e^2 |M_{96}|^2}{\lambda e_0 n_w L_p (2\gamma_{96})} [n_9 - n_6 - (n_9 - n_6)_{th}], \tag{3.22}$$

where λ is the lasing wavelength at w, n_w is refractive index at the fundamental frequency, L_p is the thickness of one period of active region and $(n_9 - n_6)_{th}$ is the threshold population inversion which is derived by setting $\frac{dn_w}{dt} = 0$ in Eq. (3.17),

$$(n_9 - n_6)_{th} = (n_{(14)} - n_{(15)})\frac{W^p_{(15)(14)}}{W^p_{96}} + (n_9 - n_{14})\frac{W^p_{(14)9}}{W^p_{96}} + 2(n_6 - n_{14})\frac{W^{2p}_{(14)6}}{W^p_{96}} + 2(n_9 - n_{15})\frac{W^{2p}_{(15)9}}{W^p_{96}} + \frac{1}{\Gamma W^p_{96}\tau^{\omega}_p} \quad . \tag{3.23}$$

Equation (3.23) also accounts for all relevant losses in the lasing cavity with SHG; the first four terms correspond to single- and two-photon absorptions, while the last term corresponds to the waveguide loss and mirror loss. Above threshold, i.e., $G^{net}_m > 0$, the medium begins to lase. The linear and SHG output light intensity can be calculated from the photon density m in the cavity as

$$I_w = N_{\mathrm{mod}}(\hbar w) m_w \frac{L}{t_m}, \tag{3.24}$$

where N_{mod} is the number of periods in the lasing cavity (the value is taken as 50 as in [16]), and the t_m is mirror photon escape time, defined by $t_m^{-1} = a_m v_g$, where a_m is the mirror loss and v_g is the group velocity. The output power is calculated by

$$P_w = I_w A \tag{3.25}$$

where A is the cross section area transverse to the light propagation direction.

With the steady-state electron population, the second-order nonlinear susceptibility $c^{(2)}$ can be evaluated as Eq. (3.6).

The initial fundamental power output can be obtained from the solution of the steady-state rate equation stated as Eqs. (3.24) and (3.25). Only the TM modes are excited efficiently since the polarization associated with electronic intersubband transitions contains only the x component. The wave propagates along the waveguide in the z direction. In order to simplify the solution procedure, It is assumed that the

transverse wave profile is only x dependent. The magnetic fields $H_{y,w(2w)}$ of the fundamental and SH modes can be represented as,

$$H_{y,\omega}(x,z) = A_{\omega}(z)F_{\omega}(x)e^{-ik_{\omega}z}, \tag{3.26a}$$

$$H_{y,2\omega}(x,z) = A_{2\omega}(z)F_{2\omega}(x)e^{-ik_{2\omega}z}. \tag{3.26b}$$

$A_{w(2w)}(z)$ is the magnetic field amplitude varying along the wave guide direction. It is assumed that $A_w(z)$ varies slowly with the coordinate z and $A_{2w}(0) = 0$. $F_{w(2w)}(x)$ represents the mode profile in the transverse direction and satisfy the Helmholtz equation,

$$\frac{\partial^2 F_{w(2w)}(x)}{\partial x^2} + \left(\frac{w^2 e_{w(2w)}(x)}{c^2} - k_{w(2w)}{}^2 \right) F_{w(2w)}(x) = 0, \tag{3.27}$$

where $e_{w(2w)}$ is the frequency and position dependent dielectric constants. The equations are solved by the finite-difference approach, in which different TM modes at both frequencies are obtained with phase constants $k_{w(2w)}$ solved as eigenvalues and transverse mode profiles $F_{w(2w)}(x)$ as eigenvectors.

The linear and nonlinear power outputs relate to the magnetic field amplitudes as,

$$P_{\omega(2\omega)}(z) = \frac{n_{\omega(2\omega)} W}{2\varepsilon_0 c} \left| A_{\omega(2\omega)}(z) \right|^2 \int \frac{F^2_{y,\omega(2\omega)}(x)}{\varepsilon_{\omega(2\omega)}(x)} dx, \tag{3.28}$$

where $W = 13mm$ is the width of the wave guide given in [16]. The transverse component of electric field E_x is related to H_y as

$$\frac{\partial H_y(x,z,w)}{\partial z} = iwe(x,w)E_x(x,z,w). \tag{3.29}$$

The transverse electric field at SH frequency is related to that at the fundamental frequency through Maxwell's coupled wave equation,

$$\frac{\partial E_{x,2\omega}(x,z)}{\partial z} = i\frac{(2\omega)^2}{4k_{2\omega}c^2}\chi^{(2)}E_{x,\omega}^2(x,z)e^{i(2k_\omega - k_{2\omega})z}. \tag{3.30}$$

By combining Eqs. (3.29) and (3.30), the magnitude of the SH magnetic field at output can be derived as,

$$A_{2\omega}(L) = \frac{\frac{n_\omega^2 \omega A_\omega^2}{2c^2\varepsilon_0}\left(\frac{e^{i\Delta\gamma L}-1}{\Delta\gamma}\right)\frac{\sqrt{1-R_2}}{1-R_1}\int\frac{1}{\varepsilon_\omega^2(x)}\chi^{(2)}(x)F_{y,\omega}^2(x)F_{y,2\omega}(x)dx}{\int F_{y,2\omega}^2(x)dx}, \tag{3.31}$$

where $n_w = k_w c/w$ and $n_{2w} = k_{2w}c/w$ are refractive indices of the fundamental and SH modes, $g_w = k_w$ and $g_{2w} = k_{2w} + ia_{2w}$, are the wavevectors of the fundamental and SH waves, a_{2w} are total loss including the waveguide loss a_{2w}^w and mirror loss a_{2w}^m for the SH mode, and $\Delta k = 2k_w - k_{2w}$ is the phase constant mismatch. Since the propagation loss a_w in the fundamental mode wave has been included in the single-photon rate equation Eq. (3.17) through the photon lifetime t_p^w, which means that the loss has been taken into account in the evaluation of the linear power P_w, it is not contained in the wavevector g_w in Eq. (3.31). The waveguide losses $a_{w(2w)}^w$ and dimensions are adopted from the experimental data in [16]. The mirror losses can be estimated by $a_{w(2w)}^m = -(\ln R_{1(2)})/L$, where R_1 and R_2 are reflection coefficients at the fundamental and SH frequencies respectively and they are related to refractive indices as $R_{1(2)} = (1-n_{w(2w)})^2/(1+n_{w(2w)})^2$.

From Eq. (3.28) and (3.31), the nonlinear output power can be obtained from linear power as,

$$P_{2w} = \frac{2p^2 \left| c^{(2)} \right|^2 \left[e^{-2a_{2w}L} - 2e^{-a_{2w}L} \cos(DkL) + 1 \right] (1 - R_2)}{I_R n_w^2 n_{2w} l_0^2 c e_0 \left(Dk^2 + a_{2w}^2 \right) (1 - R_1)^2} P_w^2, \tag{3.32}$$

where l_0 is the wavelength of the fundamental mode and I_R is the effective interaction cross section decided by the overlap between the fundamental mode and SH mode,

$$I_R = \frac{1}{n_w^4 n_{2w}^2} \frac{\left(\int F_{2w}^2(x) dx \right)^2 \left(\int \frac{1}{e_w(x)} F_w^2(x) dx \right)^2 W}{\left(\left| \int \frac{1}{e_w^2(x)} c^{(2)}(x) F_w^2(x) F_{2w}(x) dx \right| \right)^2 \int \frac{1}{e_{2w}(x)} F_{2w}^2(x) dx}. \tag{3.33}$$

In the simulation, I_R is estimated to be 470 μm^2, which is about half of that reported in [16]. This is due to the assumption that $c^{(2)}$ is uniformly distributed in the nonlinear interaction region. This assumption is valid as the current study emphasizes on the relative enhancement effect of the SUSYQM optimized structure over the original structure. In Eq. (3.32), since the phase-mismatch factor Δk is about 100 times larger than loss a_{2w}, the SH power will be decreased about 10^{-4} of the power under phase-matching condition. If the phase mismatching can decrease to a value around the loss value, the SH power can thus be improved 10^3 to 10^4 times larger.

3.3.4 Comment on Intersubband Refractive Index

From Eqs. (3.24) and (3.33), the variation of refractive indices $n_{w(2w)}$ have substantial influence on the lasing performance. Apart from the fixed bulk refractive indices, there are also contributions due to intersubband transitions [53], which are related to the intersubband linear susceptibility $c^{(1)}$ for and bulk refractive index $n_b(w)$ as

$$n_{isb}(w) = \text{real}\left[c^{(1)}(w) \right] / 2 n_b(w), \tag{3.34}$$

where, for the bandstructure shown in Fig. 3.2, $c^{(1)}$ is evaluated as,

$$c^{(1)}(w) \approx \frac{4pe^2}{e_0}\left[\frac{(n_2 - n_3)M_{23}^2}{(E_{32} - \hbar w) - ig_{32}} + \frac{(n_3 - n_4)M_{34}^2}{(E_{43} - \hbar w) - ig_{43}} + \frac{(n_4 - n_5)M_{45}^2}{(E_{54} - \hbar w) - ig_{54}}\right]. \qquad (3.35)$$

It can be seen from Eq. (3.35) that $c^{(1)}$ is related to the intersubband radiative transitions.

Calculation results show that intersubband refractive index is smaller than 0.2 % of the bulk refractive index and the influence is ignored. The reason is that competitions among radiative transitions between each pair of resonant levels suppress the overall influence from the whole active region.

3.4 Optimization Effects on Linear and Nonlinear Output Performances

The current-density variation with the applied electric field for the original and optimized structures are shown in Fig. 3.7. It can be seen that the current flow in the optimized structure is more sensitive to the applied field, in which negative differential resistance (NDR) can be observed. This can be attributed to the band-structure variation with the applied bias, which is completely decided by the geometry and material composition of the multiple QW's. For both structures, the highest current flow happens at the cascading bias 38 kV/cm due to the strong resonant tunneling between the active and injector/collector regions. At this bias, one level in the miniband of the injector/collector region is closely aligned with the upper lasing level or lower lasing level in the active region. Below this point, the current in the optimized structure ramps up faster with the applied bias. When the applied bias increases above 38 kV/cm, current in the optimized structure drops quickly and then ramps up again. This happens when another level in the miniband of the injector/collector region is aligned with the upper/lower lasing level in the active region. For the original structure, there is only a mild change of the band

structure with the applied bias. The tunneling enhancement due to this optimization is not explicitly addressed in the optimization approach, but is rather a serendipitous outcome of the optimization.

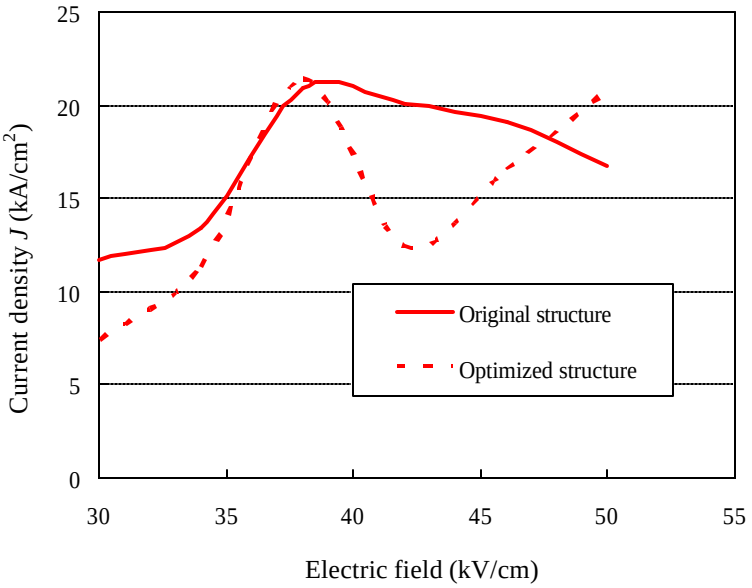

Figure 3.7 The current flow through injector-active region-collector versus the applied voltage for both the original and optimized structures.

The improvement in the SHG might be expected to affect adversely the gain due to the population competition among lasing levels and the nonlinear cascades. The increased oscillator strength, however, between lasing levels tends to counter this competition. Figure 4 shows the net modal gain for the original structure and optimized structure. It can be seen that the optimized structure has a lower threshold current than the original structure. Adopting the numbers given in Ref. [16], the lasing cavity is 13 μm wide and 2.25 mm long. The threshold current for the optimized structure is 1 A corresponding to a current density of 3.4 kA/cm^2, while that for the original structure is about 6.8 kA/cm^2. Above threshold, when the linear output power rises beyond the saturation power, the gain begins to drop until it equals the total loss. This corresponds to

zero net modal gain, as shown Fig. 3.8(a). With zero net modal gain, the output power is in steady-state. When the power falls below the saturation power, the modal gain increases linearly with the current flow and the optimized structure has a higher modal gain/current slope, as shown in Fig. 3.8(b).

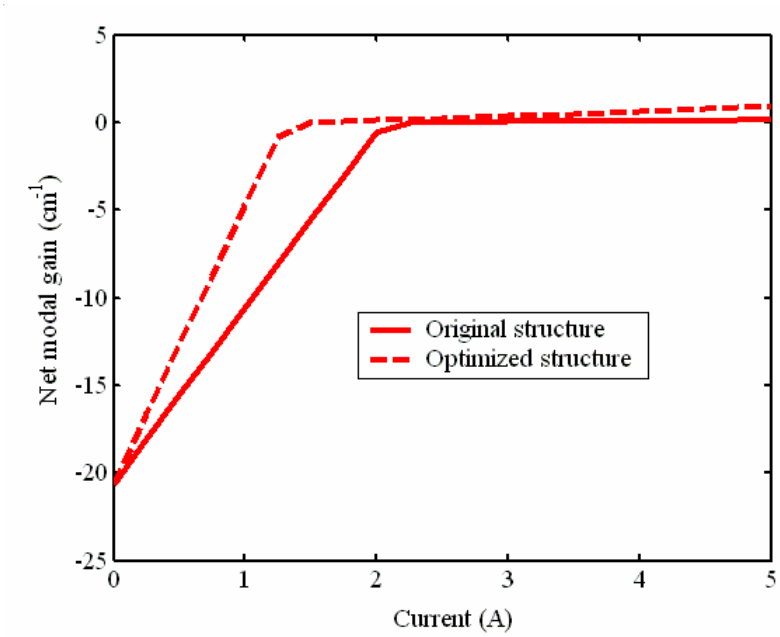

(a)

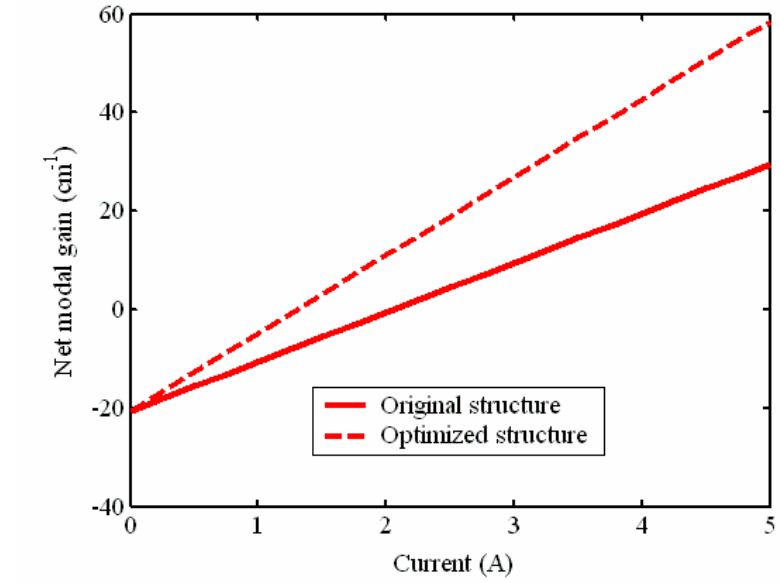

(b)

Figure 3.8 Net modal gain versus current for the original and optimized structures: (a) above saturation; (b) below saturation.

Figure 3.9 shows the variation of $|c^{(2)}|$ with pumping current for both the original structure and optimized structure. Eq. (3.6) tells that $|c^{(2)}|$ are dependent on both the dipole matrix element products and the population distribution on the states of the active region. It shows that $|c^{(2)}|$ for the optimized structure is about 1.5 times of that of the original structure which is about the improvement of the dipole matrix element product $M_{23}M_{34}M_{24}$ for the first SHG cascade. $|c^{(2)}|$ changes slowly with the pumping current above threshold condition.

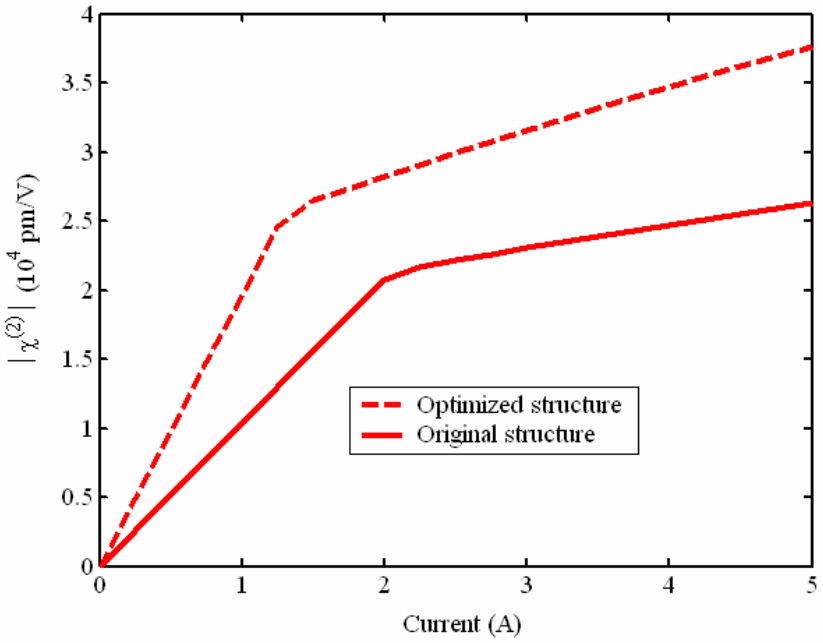

Figure 3.9 Variation of second-order nonlinear susceptibility under different pump current.

Figure (3.10) shows the linear and nonlinear output for both the original and optimized structure. The nonlinear power output is calculated under phase-mismatched condition. The higher oscillator strength between the lasing levels in the optimized one leads to higher stimulated emission rate and makes higher linear power output. For the

original structure, the highest linear power is 380 mW, the nonlinear power is 85 μW. These correspond to a linear to nonlinear conversion efficiency of 603 μW/ W^2. This is close to the results shown in Ref. [16]. In the optimized structure, the numbers increase to 490 mW linear power and 323 μW nonlinear power, which correspond to 1300 μW/W^2 linear to nonlinear conversion efficiency. The mode profiles of the TM_{00} mode at fundamental frequency and three modes at SH frequency are shown in Fig. 3.11, in which "FM" represent fundamental mode. In the following calculations, the TM_{00} modes are picked up at both frequencies since simulation results based on them are much closer to the experimental measurements reported in Ref. [16]. It was found that better phase-matching can be achieved between TM_{00} mode at fundamental frequency and TM_{02} mode at SH frequency, which is the same conclusion as Malis, *et al.* [54]. With the optimized design, the linear-to-nonlinear conversion efficiency can achieve a twofold enhancement over the original one. The calculation shows that the nonlinear power output is only 10^{-4} of that under phase-matched conditions. Even though the phase-mismatched condition didn't degrade the enhancement of SHG by optimization, the phase-matched condition is a very crucial factor to improve the linear to nonlinear conversion efficiency in QCL structure. However, that technique is a different physical concept as the optimization technique, which provides a means to improve the nonlinearity of the lasing medium.

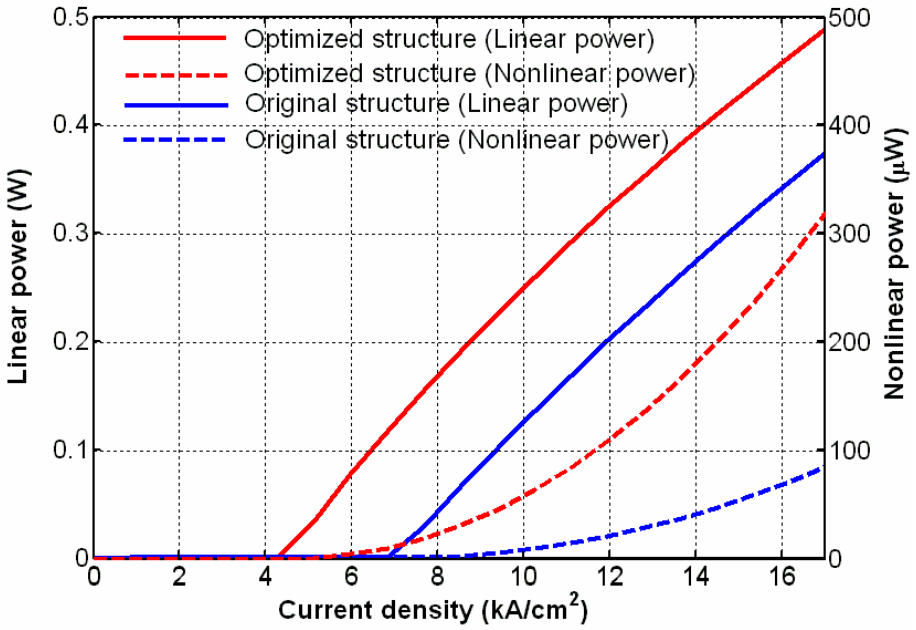

Figure 3.10 Fundamental power and nonlinear power under different pump current.

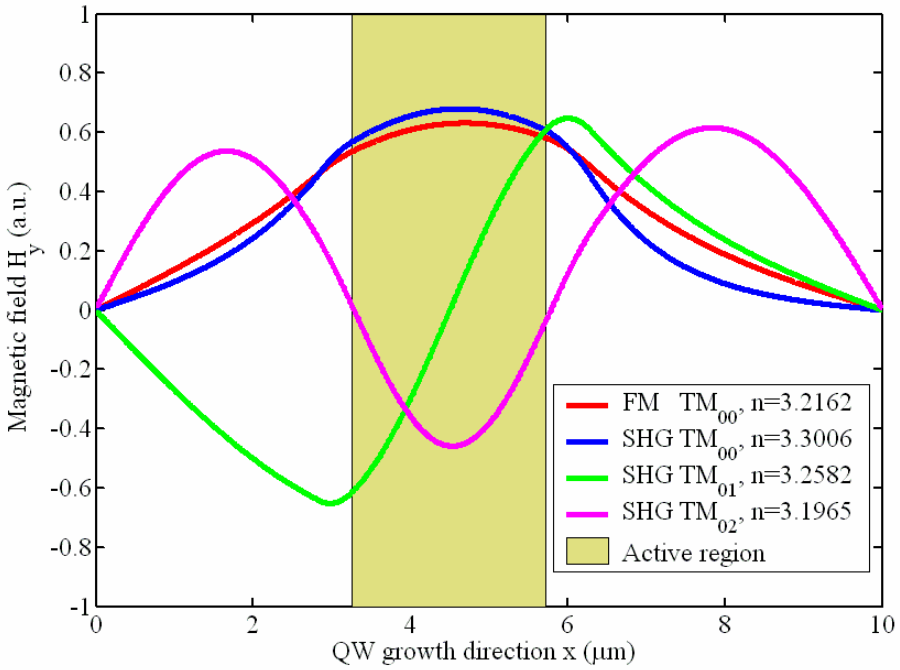

Figure 3.11 Transverse magnetic field profiles at the fundamental frequency and second-harmonic frequency.

CHAPTER 4

THIRD-ORDER OPTICAL NONLINEARITIES OF QUANTUM CASCADE LASERS

In this chapter, further study on the third-order optical nonlinearities is carried out on the structure shown in Fig. 3.2, which is a MIR QCL with a pair of triply harmonic resonant levels. Potential applications of such design are discussed based on the resonant third-order nonlinear susceptiblility $c^{(3)}$ at the TH) frequency, $c^{(3)}(3w;w,w,w)$, and that at fundamental frequency $c^{(3)}(w;w,w,-w)$, which is described in Eq. (1.4). The TH power generated is evaluated based on $c^{(3)}(3w;w,w,w)$, mode overlap with the fundamental mode and the effect of phase mismatch. The higher-order TH mode with the best phase-matching to the fundamental is identified, which greatly improves the linear to TH conversion efficiency. In addition to single-photon processes, resonant two-photon processes are included in the evaluation of $c^{(3)}(w;w,w,-w)$, which results in the enhancement of the positive nonlinear refractive index which is predicted to enable the ultrashort pulse generation via SML. It is concluded that QCL's with multiple-resonance design are not only favorable for tunable light emission at the SH and TH frequencies in the NIR to MIR region, but are also promising candidates for ultrafast compact long-wavelength lasers.

4.1 Third-Harmonic Generation

THG is associated with the processes illustrated in Fig. 4.1 (a), in which three photons with frequency w are destroyed and one photon with frequency $3w$ is created; $c^{(3)}(3w;w,w,w)$ is a figure of merit of THG. It is expressed as [41],

$$c^{(3)}(3w;w,w,w)=\frac{4pq^4M_{23}M_{34}M_{45}M_{25}}{e_0(E_{52}-3\hbar w-ig_{52}/2)}\left[\frac{1}{E_{42}-2\hbar w-ig_{42}}\left(\frac{n_3-n_4}{E_{43}-\hbar w-i(g_{43}/2)}+\frac{n_3-n_2}{E_{32}-\hbar w-ig_{32}}\right)\right.$$
$$\left.\frac{1}{E_{53}-2\hbar w-ig_{53}}\left(\frac{n_4-n_5}{E_{54}-\hbar w-ig_{54}}+\frac{n_4-N_5}{E_{43}-\hbar w-ig_{43}}\right)\right]. \quad (4.1)$$

$c^{(3)}(3w;w,w,w)$ can be evaluated based on the rate-equation solutions presented in Chapter 3.3.3.

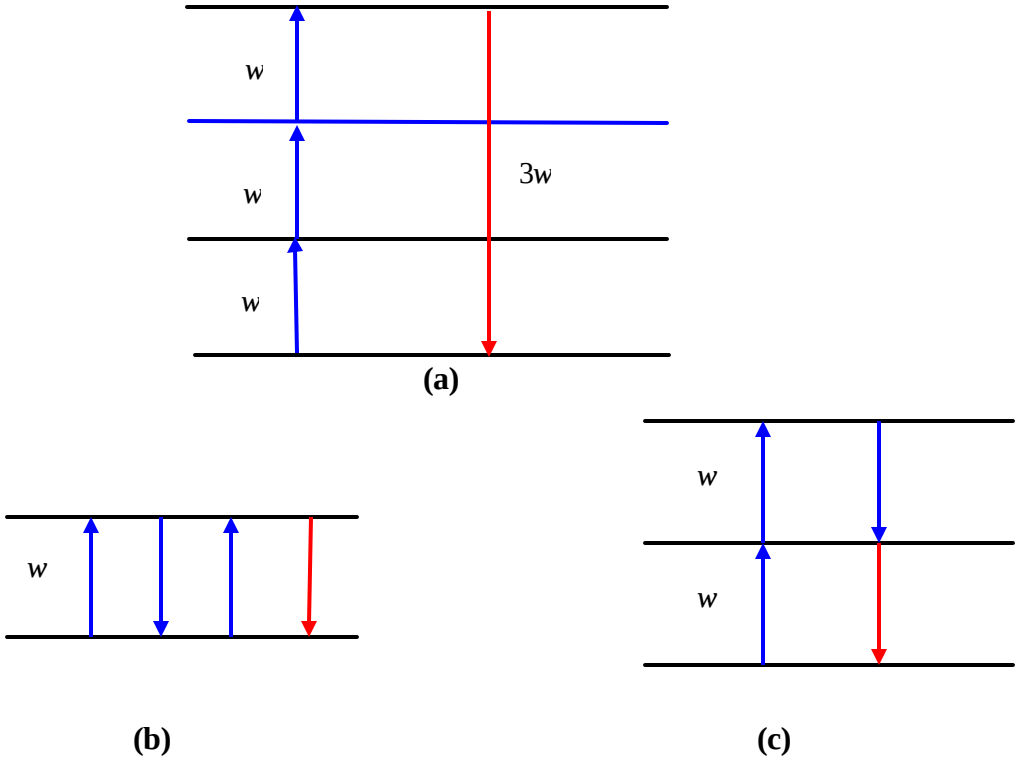

Figure 4.1 Illustration of different resonant transitions: (a) third-harmonic generation; (b) single-photon process; (c) two-photon process.

The initial fundamental power output can be obtained from the steady-state photon populations as in Eqs. (3.24) and (3.25). Only TM modes are excited efficiently since the polarization associated with electronic intersubband transitions contains only the growth-oriented x component. The wave propagates along the waveguide in the longitudinal z direction. In order to simplify the solution procedure, it is assumed that the transverse mode profile is only x dependent. The magnetic fields $H_{y,\omega(3\omega)}$ of the fundamental and TH modes can be represented as

$$H_{y,\omega}(x,z) = A_{\omega}(z)F_{\omega}(x)e^{-ik_{\omega}z}, \tag{4.2a}$$

$$H_{y,3\omega}(x,z) = A_{3\omega}(z)F_{3\omega}(x)e^{-ik_{3\omega}z}. \tag{4.2b}$$

Here, $A_{\omega(3\omega)}(z)$ is the magnetic-field amplitude varying along the waveguide direction. It is assumed that that $A_w(z)$ varies slowly with coordinate z and $A_{3\omega}(0) = 0$. $F_{\omega(3\omega)}(x)$ represents the mode profile in the transverse direction and satisfies the Helmholtz equation,

$$\frac{\partial^2 F_{w(3w)}(x)}{\partial x^2} + \left(\frac{w^2 e_{w(3w)}(x)}{c^2} - k_{w(3w)}{}^2 \right) F_{w(3w)}(x) = 0, \tag{4.3}$$

where $e_{w(3w)}$ is the frequency- and position-dependent dielectric constants. The equations are solved by the finite-difference approach, in which the TM modes at both frequencies are obtained with phase constants $k_{\omega(3\omega)}$ solved as eigenvalues and transverse mode profiles $F_{\omega(3\omega)}(x)$ as eigenvectors.

The linear and nonlinear power outputs relate to the magnetic field amplitudes as

$$P_{\omega(3\omega)}(z) = \frac{n_{\omega(3\omega)}W}{2\varepsilon_0 c}\left|A_{\omega(3\omega)}(z)\right|^2 \int \frac{F^2_{y,\omega(3\omega)}(x)}{\varepsilon_{\omega(3\omega)}(x)}dx, \tag{4.4}$$

where $W = 13mm$ is the width of the wave guide given in [16]. The transverse component of electric field E_x is related to H_y as

$$\frac{\partial H_y(x,z,w)}{\partial z} = iwe(x,w)E_x(x,z,w). \tag{4.5}$$

The transverse electric field at the TH frequency is related to that at the fundamental frequency through the wave equation,

$$\frac{\partial E_{x,3w}(x,z)}{\partial z} = i\frac{(3w)^2}{4k_{3w}c^2}c^{(3)}E_{x,w}^3(x,z)e^{i(3k_w-k_{3w})z}. \tag{4.6}$$

With the combination of Eqs. (4.5) and (4.6), the magnitude of the TH magnetic field at output can be expressed as

$$A_{3\omega}(L) = \frac{\frac{3n_\omega^3\omega A_\omega^3}{4c^3\varepsilon_0^2}\left(\frac{e^{i\Delta\gamma L}-1}{\Delta\gamma}\right)\frac{\sqrt{1-R_3}}{(1-R_1)^{3/2}}\int\frac{1}{\varepsilon_\omega^3(x)}\chi^{(3)}(x)F_{y,\omega}^3(x)F_{y,3\omega}(x)dx}{\int F_{y,2\omega}^2(x)dx}, \tag{4.7}$$

where $n_w = k_w c/w$ and $n_{3\omega} = k_{3\omega}c/(3\omega)$ are the fundamental and TH modal refractive indices, $g_w = k_w$ and $\gamma_{3\omega} = k_{3\omega} + i\alpha_{3\omega}$ are the wavevectors of the fundamental and TH waves, $\alpha_{3\omega}$ is the total loss including the waveguide loss and mirror loss for the TH wave, $\Delta k = 3k_\omega - k_{3\omega}$ is the phase constant mismatch, and R_1 and R_3 are the reflection coefficients at fundamental and TH frequencies.

From Eqs. (4.6) and (4.7), the nonlinear output power can be obtained from linear power as

$$P_{3w} = \frac{9p^2\left|c^{(3)}\right|^2\left[e^{-2a_{2w}L} - 2e^{-a_{2w}L}\cos(\Delta kL)+1\right](1-R_3)}{I_3^2 n_w^3 n_{2w} l_0^2 ce_0^2\left(\Delta k^2 + a_{2w}^2\right)(1-R_1)^3}P_w^3, \tag{4.8}$$

where I_3 is the effective interaction area determined by the overlap between the fundamental wave and TH waves,

$$I_3 = \frac{W}{n_\omega^3 n_{3\omega}^1} \frac{\left(\int F_{3\omega}{}^2(x)dx\right)\left(\sqrt{\int \frac{1}{\varepsilon_\omega(x)} F_\omega{}^2(x)dx}\right)^3}{\left(\left|\int \frac{1}{\varepsilon_\omega^3(x)} \chi^{(2)}(x) F_\omega{}^3(x) F_{3\omega}(x)dx\right|\right)\sqrt{\int \frac{1}{\varepsilon_{3\omega}(x)} F_{3\omega}{}^2(x)dx}}, \tag{4.9}$$

From Eq. (4.8), it can be observed that TH power output is proportional to $\left|c^{(3)}(3w;w,w,w)\right|^2$. In addition, the mode-profile overlap and phase mismatch also play important roles. In our simulations, the emission powers at the fundamental, SH and TH frequencies are compared. The calculation of SH power follows procedures given in Section 3.3.3.

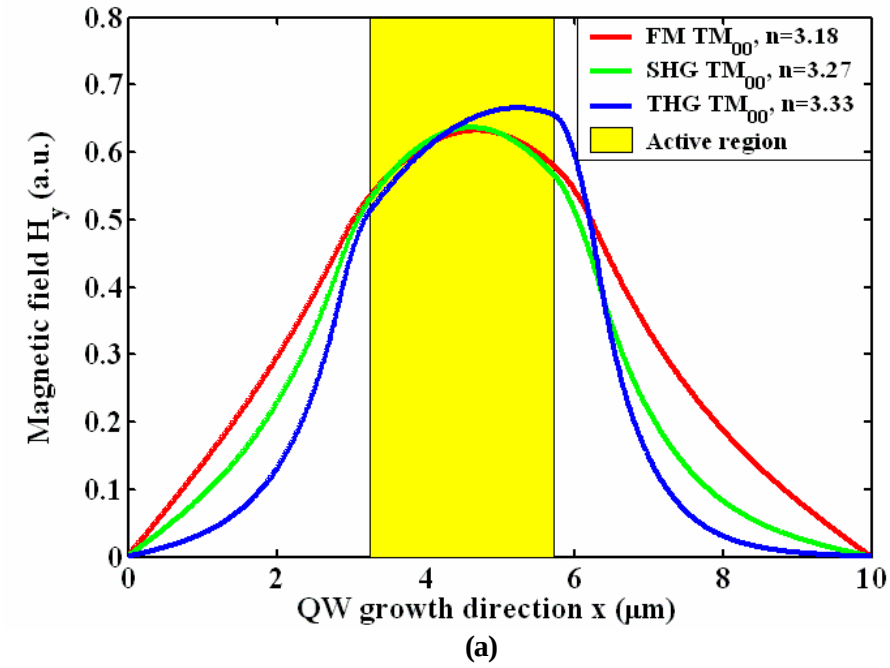

(a)

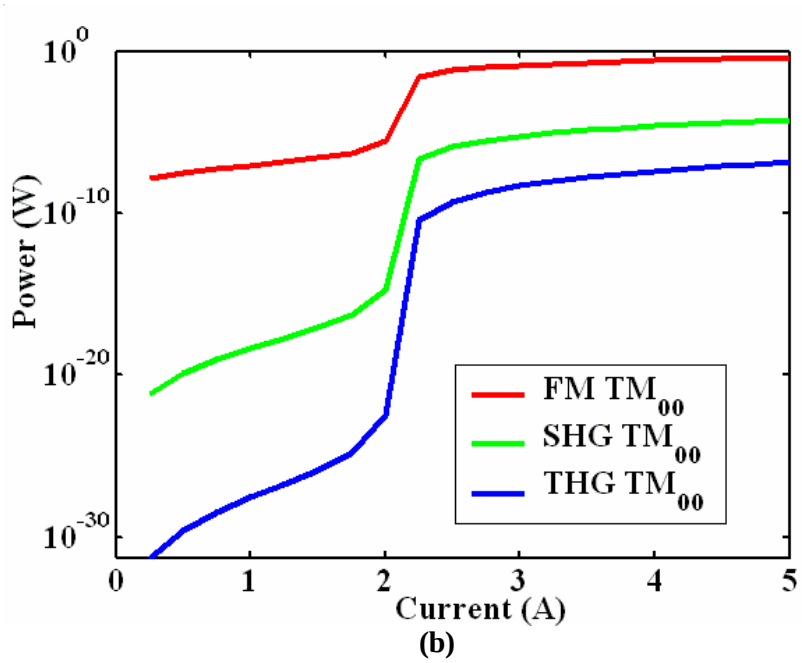

Figure 4.2 Lowest order of fundamental, second-harmonic, and third-harmonic modes: (a) mode profiles; (b) power outputs.

The maximum overlap between the SH/TH mode and the fundamental mode occurs for the lowest mode TM_{00} at those three frequencies, whose profiles are shown in Fig. 4.2(a) and the corresponding emission powers are shown Fig. 4.2(b). From Eq. (4.8), it can be seen that the mode overlap is inversely proportional to the effective interaction area. To achieve higher SH/TH output power, the interaction area should be as small as possible. The effective interaction area for the SH mode is 470 μm^2, with maximum SH emission up to 85 μw; the effective area or the TH mode is 123 μm^2 with maximum TH emission as 135 nW. The linear to SHG conversion efficiency $h_{2w} = P_{2w}/P_{2w}^2$ is 603 $\mu W/W^2$, while the linear to THG conversion efficiency $h_{3w} = P_{3w}/P_w^3$ is 2.6 $\mu W/W^3$. These numbers are close to the experimental results reported in [16, 55]. The deviation is likely in part due to the assumption that the nonlinear susceptibilities are constant within the active region. It was found that higher orders of SH and TH modes have better phase-

matching with the TM_{00} fundamental mode. As shown in Fig. 4.3(a), the best phase-matching could be achieved between TM_{02} SH /TM_{04} TH modes and the TM_{00} fundamental mode, but with some sacrifice of mode profile overlap. The effective interaction cross-section between TM_{02} SH and TM_{00} fundamental modes increases to 568 μm^2, and the maximum SH power output is 1.2 mW; the effective cross-section between TM_{04} TH and TM_{00} fundamental modes increases to 233 μm^2, and the maximum TH power output is 1.0 μw. Under the best phase-matching condition, even though with the reduced mode overlap, there is nonetheless still a 20-fold improvement for the SH power and a 10-fold improvement for the TH power. Therefore, phase-matching is the most crucial factor for achieving higher powers in the harmonics.

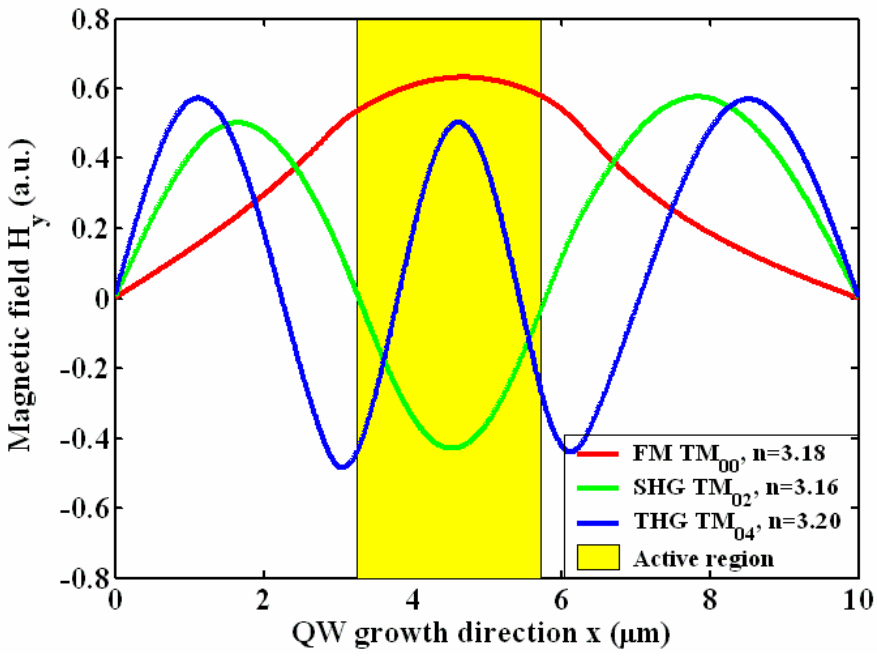

(a)

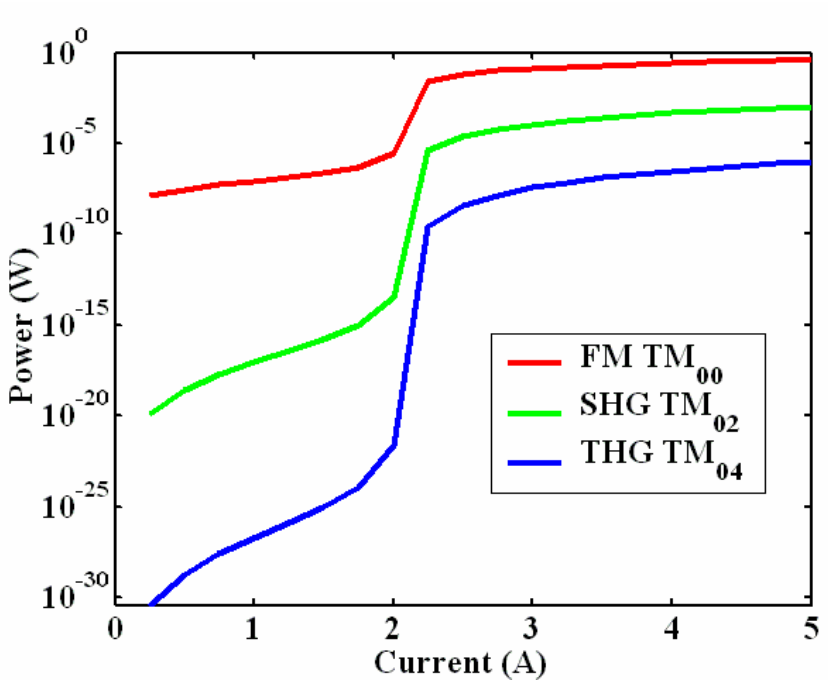

(b)

Figure 4.3 Second-harmonic and third-harmonic modes with the best phase-matching to the fundamental mode: (a) mode profiles; (b) power outputs.

4.2 Nonlinear Refractive Index with Harmonic Resonant Levels

The second term in Eq. (1.4) describes a nonlinear contribution to the polarization at the fundamental frequency w. This leads to a nonlinear contribution to the refractive index (Kerr effect) at frequency w. The refractive index including the Kerr nonlinearity can be expressed as [42]

$$n_w = n_0 + n_2 I \tag{4.10}$$

where n_0 is the linear refractive index, n_2 is the nonlinear refractive index,

$$n_2 = \frac{3}{4n_0^2 e_0 c}\mathrm{Re}\left[c^{(3)}(w;w,w,-w)\right], \tag{4.11}$$

and the light intensity is $I = \frac{1}{2} n_0 c e_0 E^2$.

In [24], SML in QCL's from the intensity-dependent refractive index has been demonstrated. If n_2 is positive, due to the Kerr-lensing effect, the central portion of the transverse beam profile, where the intensity is highest, experiences a larger refractive index relative to the edges. Thereafter, the nonlinear dielectric waveguide increases the beam confinement near its center and narrows the beam diameter to an extent proportional to the optical power. In the presence of such a mechanism, the mode interaction with external metal contact decreases and thus reduces the optical losses. This is a favorable mechanism for the laser to emit ultrashort pulses. Even though we did not estimate the pulse duration here due to the lack of experimental data for the root-mean-square of the spectral width, it can be inferred qualitatively the enhancement of SML effect by analyzing the n_2 variation due to the additional harmonic resonance levels.

Following Eq. (4.11), n_2 can be obtained from $c^{(3)}(w;w,w,-w)$, which itself can be evaluated based on the steady-state rate-equation solutions described in Section 3.3. For the bandstructure shown in Fig. 1.1, according to formulation derived in [42], two kinds of resonant terms contribute to $c^{(3)}(w;w,w,-w)$, i.e., terms related to single-photon processes as shown in Fig. 1(b) and those related to two-photon process as in Fig. 1(c),

$$c^{(3)}(w;w,w,-w) = c_{1p}^{(3)}(w;w,w,-w) + c_{2p}^{(3)}(w;w,w,-w). \tag{4.12}$$

Single-photon transitions exist between any two states whose separation is resonant with the fundamental frequency w, i.e. states $E_2 - E_3$, $E_3 - E_4$ and $E_4 - E_5$. For any lasing structure there is single-photon processes contributing to $c^{(3)}(w;w,w,-w)$,

which leads to absorption saturation. The explicit expression of $c^{(3)}(w;w,w,-w)$ by summing up all the contributions from the single-photon processes is

$$c_{1p}^{(3)}(w;w,w,-w)=\frac{8pq^4}{3e_0}\left[(N_3-N_2)\frac{M_{23}^4}{(E_{32}-\hbar w-ig_{32})^2(E_{32}-\hbar w+ig_{32})}\right.$$
$$+\ (N_4-N_3)\frac{M_{43}^4}{(E_{43}-\hbar w-ig_{43})^2(E_{43}-\hbar w+ig_{43})} \qquad (4.13)$$
$$\left.+(N_5-N_4)\frac{M_{54}^4}{(E_{54}-\hbar w-ig_{54})^2(E_{54}-\hbar w+ig_{54})}\right],$$

from which it can be seen that $c_{1p}^{(3)}(w;w,w,-w)$ depends on the population inversion between resonant levels, the dipole transition strength as well as the detuning and broadening factors. Due to the multiple resonance nature of the bandstructure, additional contributions to $c^{(3)}(w;w,w,-w)$ from two-photon processes also exist for resonant cascades $E_2-E_3-E_4$ and $E_3-E_4-E_5$, where two photons with frequency w are absorbed simultaneously or sequentially and stimulate the upward electronic transitions across two consecutive resonant levels $E_2\rightarrow E_4$ or $E_3\rightarrow E_5$. The expression for resonant contributions due to these two-photon processes is

$$c_{2p}^{(3)}(w;w,w,-w)=\frac{8pq^4}{3e_0}\left[N_2\frac{M_{23}^2M_{34}^2}{(E_{32}-\hbar w-ig_{32})^2(E_{42}-2\hbar w-ig_{42})}\right.$$
$$\left.+N_3\frac{M_{34}^2M_{45}^2}{(E_{43}-\hbar w-ig_{43})^2(E_{53}-2\hbar w-ig_{53})}\right]. \qquad (4.14)$$

Figure 4.4 shows the nonlinear refractive index n_2 resulting from the single- and two-photon processes, respectively, together with the total n_2 that results. The two kinds of contributions are both positive and of comparable magnitude, which means that the additional harmonic resonant levels in the lasing active region significantly enhance (actually double) the intensity-dependent refractive index, which thus is predicted to lead

to the enhancement of SML. The maximum optical intensity at the fundamental lasing frequency is about 1 MW/cm^2. This will result in a total refractive index change $Dn_w = 0.005$. The maximum nonlinear phase shift $\Delta f_{NL}^{(\max)}$ calculated from Eq. (2.49) is $\Delta f_{NL}^{\max} = 4.5p$.

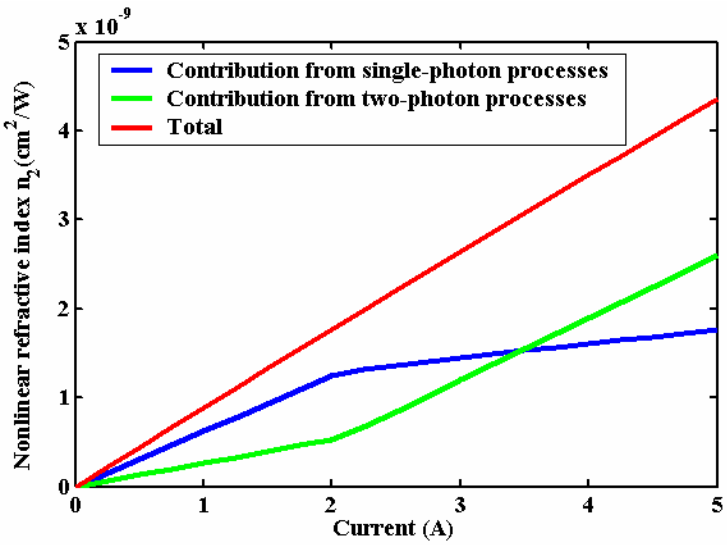

Figure 4.4 Nonlinear refractive indices due to single- and two-photon processes.

The pulse duration can be estimated from the SPM described in Section 2.4.3. Assume the pulse is in Gaussian shape and the intensity in time domain can be described as,

$$I(t) = I_0 e^{-(t/s)^2}, \tag{4.15}$$

where I_0 is peak intensity and s is the $1/e$ half-width, which is related to the FWHM pulse duration as

$$t_{FWHM} = 2\sqrt{\ln 2}s \ . \tag{4.16}$$

According to the Fourier transform of the Gaussian pulse [56],

$$Dw_0.s = 1 \tag{4.17}$$

where Δw_0 is the $1/e$ half-width in the frequency domain. The spectral broadening factor Dw_{rms} for the Gaussian pulse is given by [41],

$$\Delta w_{rms} = \sqrt{1+\frac{4}{3\sqrt{3}}\left(f_{NL}^{\max}\right)^2}\,\Delta w_0 . \tag{4.18}$$

The spectral broadening factor for structure with harmonic levels is estimated to be $\Delta w_{rms} \approx 12\Delta w_0$ while that for the QCL's structure without harmonic resonant levels is $Dw_{rms} \approx 6Dw_0$. So the increased nonlinear refractive index due to the harmonic design leads to two-fold enhancement of spectral broadening. SPM alone does not modify the pulse envelop, but a much shorter pulse can be created with the extra bandwidth generated, as follows from the Fourier transform of the wider spectrum [57]. It is strongly indicative that QCL structures with harmonic resonance design are potential candidates for ultrafast pulse generation. The enhanced spectral broadening may even shorten the pulse duration, the theoretical reasoning of which is worth continuing investigation and suggested to be one of the future research directions.

CHAPTER 5

CONCLUSIONS

This dissertation presents investigations on the optical nonlinearities of QCL's. It is based on an InGaAs/AlInAs MIR QCL with enhanced SHG in the literature. An analytical model is built for optimization of SHG followed by the performance evaluation through optoelectronic transport analysis. In addition, the THG as well as the nonlinear refractive index induced by the third-order nonlinear susceptibilities is discussed based on results from the model.

The nonlinear susceptibility associated with SHG was optimized by SUSYQM approach. Both the position and energy dependent effective mass is included in the optimization. The optimized structure can be fabricated by the state-of-art digital growth with half monolayer DP, which is much simpler than continuously grading the composition and can assure the optimization effect in some extent, while digital-growth with monolayer DP is predicted to be too coarse to approximate the ideal potential profile. The structure is partially strained but strain compensated for a period of the QCL. Lattice mismatch is included through the deformation potential.

The performance analysis of the QCL's targeting at evaluating the optimization effect is carried out semiclassically by the self-consistent rate equations. In order to account for nonideal injection efficiency within each period of the QCL, the simulation is based on a full cascade structure containing the injector, active region, and collector. By incorporating the two-photon process into the self-consistent rate equations, the modal gain, output linear power, and SHG power can be obtained from the steady-state solution

and Maxwell's wave equations. The current flowing in the entire structure in response to the applied bias is obtained through the steady-state carrier populations and scattering rates. It is found that the current density in the optimized structure responds more sensitively to the applied bias due to enhanced NDR. This may lead to highly nonconventional transport characteristics of such structures, and may be exploited outside of the context of intracavity nonlinearities in QCL's. An improvement by a factor of 2.65 of the linear-to-nonlinear conversion efficiency is expected in the ideally optimized structure, while it is 2.0 for the structure approximated by submonolayer supperlattices. The optimized structure also demonstrated the increased modal gain at the fundamental frequency and lower threshold current. In order to account for the phase mismatch influence on the nonlinear performance, wave coupling during propagation is studied with the aid of Maxwell wave equation. The linear power is enhanced and nonlinear power is suppressed under phase-mismatched condition, which accounts for about a 10^4 times reduction of the linear-to-nonlinear efficiency. This gives an indication that phase matching is an important factor in improving the nonlinear performance of the QCL structures. The supersymmetric optimization procedure is an efficient technique to achieve higher nonlinearity of the lasing medium itself. It may be pointed out that growth of the optimized structure may be difficult; nonetheless, improvements may make it worth the effort. In addition, theoretical demonstration of the effect is of interest in its own right.

Since the structure under investigation could possibly possess interesting third-order nonlinearities due to three harmonic levels, additional analysis is carried out for diverse optical nonlinearities related to $c^{(3)}$ i.e., THG and intensity-dependent refractive

index n_2. Wave-propagation analysis shows that the TH power can be greatly enhanced in higher TM modes due to better phase-matching. Because of additional contributions from resonant two-photon processes, the nonlinear refractive index is almost double that expected for a structure with only one pair of resonant levels, which results in significate spectral broadening. This is expected to result in enhanced SML leading to ultrashort pulse generation. The current work demonstrates that QCL's with optimized third-order nonlinearities promise applications in both tunable light emission and ultrafast optics. Continnued work is underway for detailed analysis on the pulse-shortening by increased nonlinear refractive index.

This work demonstrates a comprehensive theoretical methodology to analyze and enhance the nonlinearities of QCL's, which can be applied for compact multiple-color emitters and ultra-short pulse generation. Besides being well-suited for analysis of QCL's, this model can also be extended to a wide range of nanoscale optoelectronic devices with multiple-band electronic structures, i.e., intermediate-band solar cells (IBSC's) and QW infrared photodetectors (QWIP's), for both linear and nonlinear performance investigations.

REFERENCES

[1] J. Faist, F. Capasso, D. L. Sivco, C. Sirtori, A. L. Hutchinson, and A. Y. Cho, "Quantum cascade laser," *Science*, vol. 264, no. 5158, pp. 553-556, 1994.

[2] R. F. Kazarinov and R. A. Suris, "Possibility of the amplification of electronmagnetic waves in semiconductor with a superlattice," *Soviet Physics – Semiconductors*, vol. 5, no. 4, pp. 707-709, 1971.

[3] D. Hofstaetter, M. Beck, T. Aellen, J. Faist, U. Oesterle, M. Illegems, E. Gini, and H. Melchior, "Continuous wave operation of a 9.3 μm quantum cascade laser on a Peltier cooler", *Applied Physics Letters*, vol.78, no. 14, pp. 1964-1966, 2001.

[4] J. Faist, F. Capasso, D. L. Sivco, S. N.G. Chu, and A. Y. Cho, "Short wavelength (λ~3.4 μm) quantum cascade laser based on strained compensated InGaAs/AllnAs", *Applied Physics Letters*, vol.72, no. 6, pp. 680-682, 1998.

[5] A. Tredicucci, C. Gmachl, F. Capasso, D. L. Sivco, A. L. Hutchinson, and A. Y. Cho, "Long wavelength supperlattice quantum cascade lasers at λ~17 μm", *Applied Physics Letters*, vol. 74, no. 5, pp. 638-640, 1999.

[6] A. Tredicucci, C. Gmachl, M. C. Wanke, F. Capasso, A. L. Hutchinson, D. L. Sivco, S. N. G. Chu, and A. Y. Cho, "Surface plasmon quantum cascade lasers at λ~19 μm", *Applied Physics Letters*, vol. 77, no. 15, pp. 2286-2288, 2000.

[7] R. Comombelli, F. Capasso, C. Gmachl, A. L. Hutchinson, D. L. Sivco, A. Tredicucci, M. C. Wanke, A. M. Sergent, and A. Y. Cho, "Far-infrared surface-plasmon quantum cascade lasers at 21.5μm and 24 μm wavelengths", *Applied Physics Letters*, vol. 78, no. 18, pp. 2620-2622, 2001.

[8] L. C. West and S. J. English, "First observation of an extremely large dipole infrared transition within the conduction band of a GaAs quantum well," *Applied Physics Letters*, vol. 46, no. 12, pp. 1156-1158, 1985.

[9] J. Khurgin, "Second-order intersubband nonlinear-optical susceptibilities of asymmetric quantum-well structures," *Journal of the Optical Society of America. B*, vol. 6, no. 9, pp. 1672-1682, 1989.

[10] M. M Choy, and R. L. Byer, "Accurate second-order susceptibility measurements of visible and infrared nonlinear crystals," *Physical Review B*, vol. 14, no. 4, pp. 1693-1706, 1976.

[11] M. K. Gurnick and T. A. De Temple, "Synthetic nonlinear semiconductors," *IEEE Journal of Quantum Electronics*, vol. 19, pp. 791-796, 1983.

[12] M. M. Fejer, S. J. B. Yoo, R. L. Byer, A. Harwit, and J. S. Harris, "Observation of extremely large quadratic susceptibility at 9.6-10.8 μm in electric field biased AlGaAs/GaAs quantum wells," *Physics Review Letters*, vol. 62, pp. 1041-1044, 1989.

[13] E. Rosencher, A. Fiore, B. Vinter, V. Berger, P. Ph. Bois, and J. Nagle, "Quantum engineering of optical nonlinearities," *Science*, vol. 271, pp. 168-173, 1996.

[14] F. Capasso, C. Sirtori, and A. Y. Cho, "Coupled quantum well semiconductors with giant electric field tunable nonlinear optical properties in the infrared," *IEEE Journal of Quantum Electronics*, vol. 30, pp. 1313-1326, 1994.

[15] A. A. Belyanin, F. Capasso, V. Kocharovsky, and M. O. Scully, "Infrared generation in low-dimensional semiconductor heterostructures via quantum coherence," *Physical Review A*, vol 63, 053803, 2001.

[16] G. Gmachl, A. Belyanin, D. L. Sivco, M. L. Peabody, N. Owschimikow, A. M. Sergent, F. Capasso, and A. Y. Cho, "Optimized second-harmonic generation in quantum cascade lasers," *IEEE journal of Quantum electronics*, vol. 39, no. 11, pp. 1345-1355, Nov. 2003.

[17] S. L. Chuang, "Introduction to the feature issue on mid-infrared quantum cascade lasers," *IEEE Journal of Quantum Electronics*, vol. 38, no.6, pp.510-510, Jun. 2002.

[18] K. Donovan, P. Harrison, and R. W. Kelsall, "Self-consistent solutions to the intersubband rate equations in quantum cascade lasers: Analysis of a GaAs/Al_xGa_{1-x}As device", *Journal of Applied Physics*, vol. 89, no. 6, 2001.

[19] D. Indjin, P. Harrison, R. W. Kelsall, and Z. Ikonic, "Self-consistent scattering theory of transport and output characteristics of quantum cascade lasers," *Journal of Applied Physics*, vol. 91, no. 11, 2002.

[20] F. Capasso, C. Gmachl, D. L. Sivco, and A. Y. Cho, "Quantum cascade lasers," *Physics Today*, vol. 55, pp. 34-40.,2002.

[21] F. Capasso, "Quantum cascade lasers: ultrahigh-speed operation, optical wireless communication, narrow linewidth, and far-infrared emission," *IEEE Journal of Quantum Electronics*, vol. 38, pp. 511-515, June 2002.

[22] J. Faist, F. Capasso, D. L. Sivco, C. Sirtori, A. L. Hutchinson, and A. Y. Cho, "Quantum cascade laser," *Science*, vol. 264, pp. 553-556, 1994.

[23] A. A. Kosterev and F. K. Tittel, "Chemical sensors based on quantum cascade lasers," *IEEE Journal of Quantum Electronics*, vol. 38, pp. 582-591, June 2002.

[24] R. Paiella, F. Capasso, C. Gmachl, D. L. Sivco, J. N. Baillargeon, A. L. Hutchinson, A. Y. Cho, and H. C. Liu, "Self-mode-locking of quantum cascade lasers with giant ultrafast optical nonlinearities," *Science*, vol. 290, no. 5497, pp. 1739-1742, 2000.

[25] A. Soibel, F. Capasso, C. Gmachl, M. L. Peabody, A. M. Sergent, R.Paiella, D. L. Sivco, A. Y. Cho, and H. C. Liu, "Stability of pulse emission and enhancement of intracavity second-harmonic generation in self-mode-locked quantum cascade lasers," *IEEE Journal of Quantum Electronics*, vol. 40, no. 3, March 2004.

[26] D. Indjin, S. Tomic, Z. Ikonic, P. Harrison, and R. W. Kelsall, V. Milanovic and S. Kocinac, "Gain-maximized GaAs/AlGaAs quantum-cascade lasers with digitally graded active region," *Applied Physics Letters*, vol. 81, no. 12, pp. 2163-2165, 2002.

[27] S. Tomic, V. Milanovic and Z. Ikonic, "Optimization of intersubband resonsant second-order susceptibility in asymmetric graded $Al_xGa_{1-x}As$ quantum wells using supersymmetric quantum mechanics," *Physical Review B*, vol. 56, no. 3, pp. 1033-1036, 1997.

[28] K. F. Brennan, *The Physics of Semiconductors*. Cambridge, UK: Cambridge University Press, 1999.

[29] K. F. Brennan and A. S. Brown, *Theory of Modern Electronic Semiconductor Devices*. New York: John Wiley & Sons, Inc., 2002.

[30] J. A. López-Villanueva, J. A. Jiménez-Tejada, A. Palma, S.R. Bolívar and J. E. Carceller, "A simple model for analyzing the effects of band non-parabolicity in nanostructures," *Semiconductor Science and Technology*, vol. 20, pp. 532-539, 2005.

[31] D. F. Nelson, R. C. Miller, and D.A. Kleinman, "Band nonparabolicity effects in semiconductor quantum wells," *Physical Review B*, vol. 35, no. 14, pp. 7770-7773, 1987.

[32] F. Capasso, A. Tredicucci, C. Gmachl, D.L.Sivco, A. L. Hutchinson, and A. Y. Cho, "High performance superlattice quantum cascade lasers," *IEEE Journal of selected topics in quantum electronics*, vol.5, no. 3, pp. 792-807, 1999.

[33] F. Capasso, C. Gmachl, R. Paiella, A. Tredicucci, A. L. Huchinson, D. L. Sivco, J. N. Baillargeon, A.Y. Cho, and H. C. Liu, "New frontiers in quantum cascade lasers and applications," *IEEE Journal of selected topics in quantum electronics*, vol. 6, pp. 931-947, 2000.

[34] F. T. Vasko and A. V. Kuznetsov, *Electronic States and Optical Transitions in Semiconductor Heterostructures*, New York, NY: Springer, Inc., 1999.

[35] R. Ferreira and G. Bastard, "Evaluation of some scattering times for electrons in unbiased and biased single- and multiple-quantum-well structures," *Physical Review B*, vol. 40, no. 2, pp.1074-1086, 1989.

[36] M. Hartig, S. Haacke, B. Deveaud, and L. Rota, "Femtosecond luminescence measurements of the intersubband scattering rate in $Al_xGa_{1-x}As/GaAs$ quantum wells under selective excitation. *Physical Review B*, vol. 54, no. 20, pp. 14269-14272, 1996.

[37] S. –C. Lee and I. Galbraith, "Intersubband and intrasubband electronic scattering rates in semiconductor quantum wells," *Physical Review B*, vol. 59, no. 24, pp. 15796-15805, 1999.

[38] P. Harrison, "The nature of the electron distribution functions in quantum cascade lasers," *Applied Physics Letters*, vol. 75, no. 18, pp. 2800-2802, 1999.

[39] J. H. Smet, C. G. Fonstad, and Q. Hu, "Intrawell and interwell intersubband transitions in multiple quantum wells for far-infrared sources," *Journal of Applied Physics*, vol. 79, no. 12, pp. 9305-9320, 1996.

[40] C. Peschke, "The impact of electron-electron interaction on electron transport in GaAs at high electric fields," *Journal of Physics: Condensed Matter*, vol. 6, no. 35, pp. 7027-7044, 1994.

[41] P. Harrison, P. Kinsler, K. Donovan, and R. W. Kelsall, "The carrier dynamics of intersubband terahertz lasers," unpublished, available at URL: http://eenweb.leeds.ac.uk/homes/PH/projects/qcl/, accessed in May 2007.

[42] R. W. Boyd, *Nonlinear Optics*. San Diego, CA: Academic Press, 2003.

[43] G. P. Agrawal, *Nonlinear Fiber Optics*. San Diego, CA: Academic Press, 2001.

[44] R. C. Iotti, and F. Rossi, "Nature of charge transport in quantum cascade lasers," *Physical Review Letters*, vol. 87, no. 14, pp. 146603 (1-4), 2001.

[45] F. Cooper, A. Khare, and U. Sukhatme, "Supersymmetry and quantum mechanics," *Physics Report* 251, pp. 267-385, 1995.

[46] V. Milanovic and Z. Ikonic, "On the optimization of resonant intersubband nonlinear optical susceptibilities in semiconductor quantum wells," *IEEE Journal of Quantum Electronics*, vol. 32, pp.1316-1323, 1996.

[47] O. Madelung, *Semiconductors—Basic Data*, Berlin; New York: Springer, 1996.

[48] J. G. Cody, D. L. Mathine, R. Droopad, and G. N. Maracas, "Application of the digital alloy composition grading technique to strained InGaAs/GaAs/AlGaAs diode

laser active regions," *The Journal of Vacuum Science and Technology B*, vol. 12, pp.1075-1077, 1994.

[49] M. H. M. Reddy, A. Huntington, D. Buell, R. Koda, E. Hall, and L.A. Coldren, "Molecular-beam expitaxy growth of high-quality active regions with strained $In_xGa_{1-x}As$ quantum wells and lattice-matched $AlxGa_yIn_{(1-x-y)}As$ barriers using submonolayer superlattices," *Applied Physics Letters*, vol. 80, 3509-3511, 2002.

[50] G. D. Sanders and Y. C. Chang, "Effects of uniaxial stress on the electronic and optical properties of GaAs-$Al_xGa_{1-x}As$ quantum wells," *Physical Review B*, vol. 32, pp.4282-4285, 1985.

[51] W. Q. Chen, S. M. Wang, T. G. Andersson, and J. Thordson, "Inverse parabolic quantum wells grown by molecular-beam epitaxy using digital and analog techniques," *Physical Review B*, vol. 48, no. 19, pp. 14264014268, 1993.

[52] J. Ohtsubo, *Semiconductor Lasers*, Verlag Berlin Heidelberg: Springer, 2006.

[53] I. Vurgaftman, J. R. Meyer, and L. R. Ram-Mohan, "Optimized second-harmonic generation in Asymmetric double quantum wells", *IEEE Journal of Quantum Electronics*, vol. 32, no. 8, pp. 1334-1346, Aug. 1996.

[54] O. Malis, A. Belyanin, C. Gmachl, D. L. Sivco, M. L. Peabody, A. M. Sergent, and A. Y. Cho, "Improvement of second-harmonic generation in quantum-cascade lasers with true phase matching", *Applied Physics Letters*, vol. 84, no. 15, pp. 2721-2723, 2004.

[55] T. S. Mosely, A. Belyanin, C. Gmachl, D. L. Sivco, M. L. Peabody, and A. Y. Cho, "Third harmonic generation in quantum cascade laser with monolithically integrated resonant optical nonlinearity," *Optics Express*, vol.12, no. 13, pp. 2972-2976, 2004.

[56] R. N. Bracewell, *The Fourier Transform and Its Applications*. New Delhi: Tata Mcgraw-Hill Publishing Company, 2003.

[57] G. Steinmyer, D. H. Sutter, L. Gallmann, N. Matuschek, and U. Keller, "Frontiers in ultrashort pulse generation: pushing the limits in linear and nonlinear optics," Science, vol. 286, pp. 1507-1512, 1999.